Models of the iron-only hydrogenase enzyme: Structure, electrochemistry and catalytic activity of $Fe_2(CO)_3$(μ-dithiolate)(μ,$κ^1$,$κ^2$-triphos)

David Unwin[a], Shishir Ghosh[a,b], Faith Ridley[a], Michael G. Richmond[c], Katherine Holt*[a] and Graeme Hogarth*[b]

[a] *Department of Chemistry, University College London, 20 Gordon Street, London, WC1H 0AJ, U.K*

[b]*Department of Chemistry, King's College London, Britannia House, 7 Trinity Street, London, SE1 1DB, U.K*

[c]*Department of Chemistry, University of North Texas, 1155 Union Circle, Box 305070, Denton, TX 76203, USA*

Abstract

A series of diiron bis(2-diphenylphosphinoethyl)phenylphosphine (triphos) complexes $Fe_2(CO)_3$(μ-dithiolate)(μ,$κ^1$,$κ^2$-triphos) (**1-4)** [dithiolate = **1** pdt; **2** edt; **3** adt (R = Bz), **4** $(SMe)_2$] have been prepared and investigated as biomimics of the diiron site of [FeFe]-hydrogenases. The triphos ligand bridges the diiron vector whilst also chelating to one iron and exist as a mixture of basal-basal-apical (**bba**) and basal-basal-basal (**bbb**) isomers which differ in the mode of chelation. In solution the **bba** and **bbb** forms do not interconvert on the NMR time scale, but the **bba** isomers are fluxional, and at low temperature four forms of **1bba** are seen as the conformations for the trigonal twist of the $Fe(CO)_2P$ centre and pdt ring-flipping are frozen. Crystallographic studies have established **bba** (pdt) and **bbb** (adt) ground state conformations and in both there is a significant deviation away from the expected eclipsed conformation (L_{ap}-Fe-Fe-L_{ap} torsion angle 0°) by 49.4 and 24.9° respectively, suggesting that introduction of triphos leads to significant strain and DFT calculations have been used to understand the relative energies of isomers. The electron rich nature of the diiron centre in **1-4** would suggest rapid protonation, but while bridging hydride complexes such as $[Fe_2(CO)_3$(μ-pdt)(μ,$κ^1$,$κ^2$-triphos)(μ-H)][BF_4] (**1H**$^+$) can be formed the process is slow. This behavior is likely a result of the high energy barrier in forming the initial (not observed) terminal hydride which requires a significant conformational change in triphos coordination. CV studies show that all starting compounds oxidize at low potentials and the addition of $[Cp_2Fe][PF_6]$ to **1** affords $[Fe_2(CO)_3$(μ-pdt)(μ,$κ^1$,$κ^2$-

triphos)][PF_6] (**1**$^+$) which has been characterised by IR spectroscopy. DFT studies suggest a ground state for **1**$^+$ with a partially rotated $Fe(CO)_2P$ moiety that yields a weak semi-bridging carbonyl with the adjacent $Fe(CO)P_2$ group. No reduction peaks are seen for **1-4** within the solvent window but **1H**$^+$ undergoes reduction at -1.7 V. All complexes act as proton-reduction catalysts in the presence of $HBF_4{\cdot}Et_2O$. For **1**, three separate processes are observed and their dependence on acid concentration has been probed, and a mechanistic scheme is proposed based on formation via a CECE process of **1(μ-H)H** which can either slowly release H_2 or be further reduced. Relative contributions of the three processes to the total current were found to be highly dependent upon the background electrolyte, being attributed to their relative abilities to facilitate proton transfer processes. While **2** and **4** show similar proton reduction behaviour, the adt complex **3** is quite different being attributed to facile protonation of nitrogen which is followed by addition of a second proton at the diiron centre.

Keywords: iron-only hydrogenase, dithiolate, diiron, triphos, fluxionality, hydride

Introduction

Hydrogenases efficiently catalyse both the reduction of protons and oxidation of hydrogen, and while there are three distinct types, by far the most widely studied are the so-called [FeFe]-hydrogenases [**1**]. The active site of these (Chart 1a) feature a diiron centre spanned by a bridging dithiolate group further ligated by three carbonyls and two cyanides, and being linked to a [4Fe-4S] cluster *via* one of the thiolate groups of the latter. Over the past 20 years there has been considerable effort expended into the development of [FeFe]-hydrogenase biomimics [**2**], however, somewhat surprisingly given the tricarbonyl nature of the enzymes active site, complexes based on an $Fe_2(CO)_3L_3$(μ-dithiolate) framework have been relatively under-explored [**3-16**], especially in comparison with those of the type $Fe_2(CO)_4L_2$(μ-dithiolate) [**17-36**]. Rauchfuss and co-workers have studied complexes of the type $Fe_2(CO)_3(\kappa^1\text{-}PR_3)(\kappa^2\text{-}dppv)$(μ-dithiolate) (R = Me, ^{i}Pr, dppv = *cis*-1,2-bis(diphenylphosphino)ethene)) [**6**] and Schollhammer and co-workers have prepared and investigated related phosphite, $Fe_2(CO)_3\{\kappa^1\text{-}P(OMe)_3\}(\kappa^2\text{-}dppe)$(μ-pdt) [**15**], and 1,10-phenanthroline, $Fe_2(CO)_3(\kappa^1\text{-}PPh_3)(\kappa^2\text{-}1,10\text{-}phen)$(μ-pdt) [**16**], complexes (Chart 1b-d). In each of these, a chelating ligand is ligated to one iron atom and the monodentate to the second.

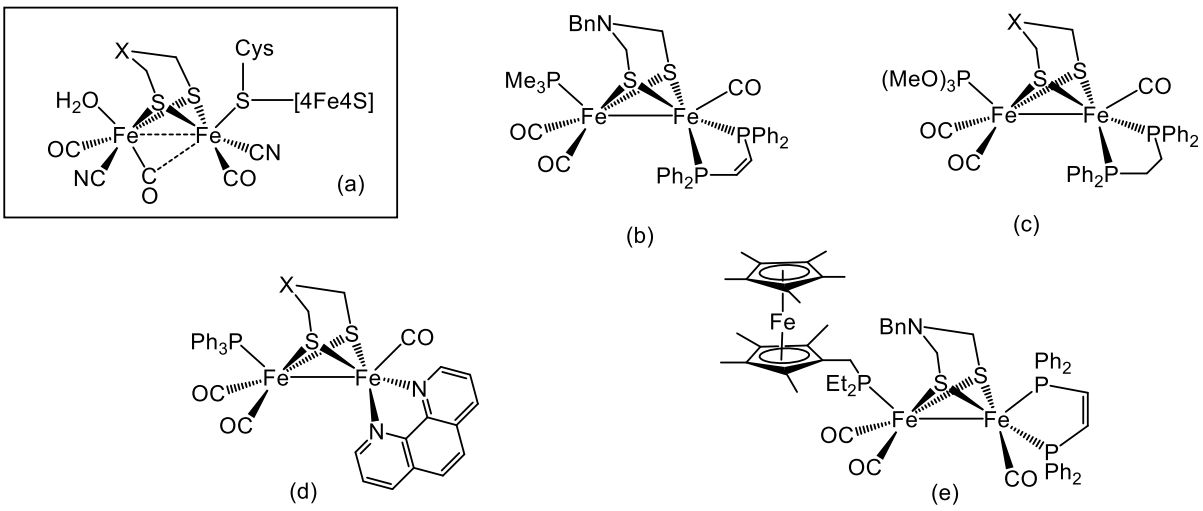

Chart. (a) Line drawing of active site of an [FeFe]-hydrogenase, (b-e) diiron tricarbonyl models previously studied

As a result of the increased electron-density at the diiron centre following multiple carbonyl substitutions, these complexes oxidise at very mild potentials making $[Fe_2(CO)_3L_3(\mu\text{-dithiolate})]^+$ readily accessible and generally protonate rapidly with even weak acids. Further, since both CO and substituted ligands are able to move between apical and basal sites, their $Fe_2(CO)_3L_3$ cores are highly flexible which can lead to significant structural rearrangements upon protonation and oxidation. For example, the addition of H^+ to $Fe_2(CO)_3(\kappa^1\text{-}PPh_3)(\kappa^2\text{-}1,10\text{-phen})(\mu\text{-pdt})$ results in rotation of the $Fe(CO)_2(PPh_3)$ moiety such that the phosphine moves from an apical to a basal site [**16**]. Likewise, oxidation of $Fe_2(CO)_3(\kappa^1\text{-}PMe_3)(\kappa^2\text{-dppv})(\mu\text{-edt})$ affords $[Fe_2(CO)_3(\kappa^1\text{-}PMe_3)(\kappa^2\text{-dppv})(\mu\text{-edt})]^+$ in which the Fe(CO)(dppv) centre rotates [**5**]. While such complexes are good models of the active enzymatic site in [FeFe] hydrogenases, similar low energy structural rearrangements might not be expected to be so facile when the diiron centre is embedded into a protein matrix. Here it is more likely that steric factors and secondary bonding interactions will significantly reduce the internal mobility of the diiron site.

With this in mind and in an attempt to limit, but not completely curtail, the structural flexibility of the diiron centre, we investigated the coordination chemistry of the tridentate phosphine, bis(2-diphenylphosphinoethyl)phenylphosphine (triphos), which can potentially both span the iron-iron bond while also chelate to one iron atom, providing a more rigid $Fe_2(CO)_3L_3$ core. In preliminary work we detailed the synthesis and molecular structure of $Fe_2(CO)_3(\mu\text{-pdt})(\mu,\kappa^1,\kappa^2\text{-triphos})$ (**1**) in which the triphos ligand spanned the diiron centre [**37**] and showed that it could

be protonated by strong acids to afford a hydride-bridged cation. Herein we present a continuation of these studies and report the synthesis of four diiron triphos complexes which differ in the nature of the dithiolate-bridge. We have also carried out detailed electrochemical and electrocatalytic studies of these complexes as proton-reduction catalysts, and the data are supported by DFT calculations, which facilitate the development of a detailed picture of their relationship to the active site of [FeFe]-hydrogenases.

Results and discussion

Synthesis and Characterization of $Fe_2(CO)_3(\mu\text{-SXS})(\mu,\kappa^1,\kappa^2\text{-triphos})$ (**1-4**) - Heating toluene solutions of $Fe_2(CO)_6(\mu\text{-SXS})$ and triphos for *ca.* 16 h resulted in isolation of the trisubstituted complexes $Fe_2(CO)_3(\mu\text{-SXS})(\mu,\kappa^1,\kappa^2\text{-triphos})$ (**1-4**) after work-up (Scheme 1). For three-atom thiolate-bridged **1** and **3** yields were high (> 90%) and work-up relatively simple. The non-linked complex, $Fe_2(CO)_6(\mu\text{-SMe})_2$, also gave a clean reaction but isolated yields were significantly lower due to the higher solubility of **4** which makes isolation more difficult. The reaction of $Fe_2(CO)_6(\mu\text{–edt})$ with triphos was quite different; a complex mixture of products resulted and **2** could only be isolated in low yields through fortuitous crystallization from CH_2Cl_2-MeOH. From IR and $^{31}P\{^1H\}$ NMR spectra of the reaction mixtures, it was clear that a range of disubstituted products with one uncoordinated phosphorus centre were also products of this reaction. A number of attempts were made to increase the yields of **2** by; prolonged heating, the addition of the oxidative-decarbonylation reagent Me_3NO and carrying out the reaction in MeCN; but all either failed to give higher yields or indeed give any of the desired product. Similarly, reactions of $Fe_2(CO)_6(\mu\text{-SAr})_2$ (Ar = Ph, *p*-tol, C_6F_5) with triphos failed to yield the targeted tricarbonyl products; the reasons for which are not known but this may be due (in part) to fragmentation into mononuclear species.

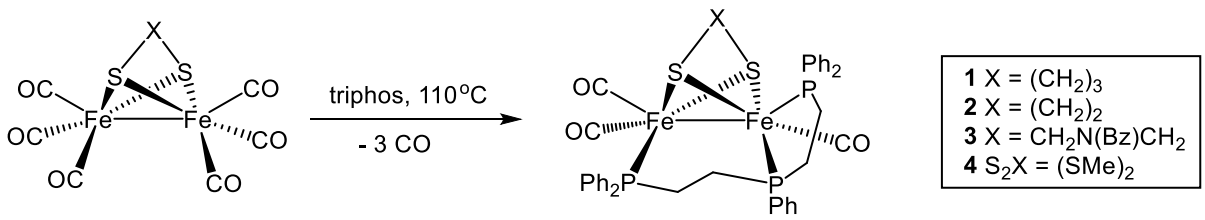

Scheme 1

Characterization of **1-4** as trisubstituted complexes was easily made on the basis of IR spectroscopy with each showing strong two carbonyl bands at *ca.* 1950 and 1890 cm^{-1}. In general, the ^{1}H NMR spectra were complex and uninformative, although the inequivalence of the two methyl groups in **4** was apparent. Most useful were $^{31}P\{^{1}H\}$ NMR spectra. For **1-3**, two isomers were observed at room temperature, each being characterized by two low-field resonances between δ 80-90 and a higher field signal between δ 60-70. We assign these to basal-basal-apical (**bba**) and basal-basal-basal (**bbb**) isomers respectively (Scheme 2), their ratios varying with the **bba** isomer predominating for **1** and **3** (ratio *ca.* 4:1), while for **2** the **bbb** isomer is the major species (ratio *ca.* 3:7). For $Fe_2(CO)_3(\mu\text{-}SMe)_2(\mu,\kappa^1,\kappa^2\text{-triphos})$ (**4**), only a single isomer was observed whose assignment was made relative to the chemical shifts of the all-basal isomer **4bbb**.

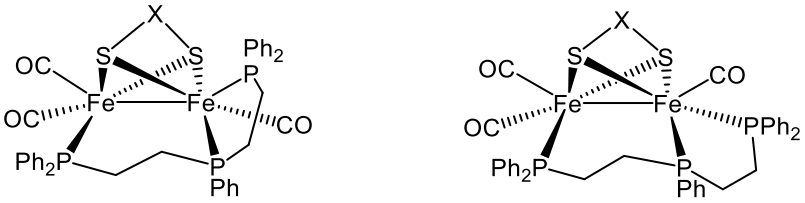

Scheme 2

Confirmation of the co-existence of **bba** and **bbb** isomers derives from the molecular structures of **1**.CH_2Cl_2 (Figure 1) [**37**] and **3.**H_2O (Figure 2) which crystallise in their **bba** and **bbb** forms, respectively. Important bond lengths and angles are summarised in Table 1 (and ESI). The triphos ligand in both products binds the diiron unit in a μ, κ^1,κ^2–fashion, bridging the diiron centre and chelating to one of the iron atoms. In **1bba**, the two chelating phosphorus atoms bind to the apical and one basal site, while in **3bbb** the ligand chelates to both dibasal sites. The angle formed by the chelate ligands at the iron mono-carbonyl centre of 88.37(3)^o and 85.35(5)^o in **1bba** and **3bbb**, respectively, and this points towards the high flexibility of this ligand. While in most complexes of the type $Fe_2(CO)_{6-n}L_n$(μ-dithiolate) the two iron centres are eclipsed (torsion angle 0^o) in both **1** and **3** there is a significant deviation from this with P_{ap}-Fe-Fe-CO_{ap} torsional angles of 49.37^o and 24.90^o respectively, showing that coordination of the triphos ligand requires some significant deviation from the prepared (eclipsed) ground state structure. These structural features may account for the low yields of **3**, the more rigid edt

ligand being less able to accommodate such changes. Coordination of triphos renders the two sulfur atoms of the dithiolate-bridge inequivalent, thus completely breaking the symmetry of the system and generating a highly asymmetric diiron centre. In both complexes, the central atom(s) of the dithiolate-bridge are orientated towards the less sterically encumbered iron dicarbonyl end of the molecule. For unlinked **4** only a single isomer was seen in the $^{31}P\{^{1}H\}$ NMR spectrum, the chemical shifts of which suggest that it is the dibasal isomer. Here there is less steric interaction between the substituents on the dithiolate groups and the triphos ligand and this presumably accounts for the observation of a single isomer in solution. While complexes of triphos have been known for over 50 years [**38**], as far as we are aware, there has only been one previously crystallographically characterised example of this ligand acting in a μ,κ^1,κ^2-fashion [**39**].

In $Fe_2(CO)_4$(μ-dithiolate)(κ^2-diphosphine) complexes, apical-basal (**ab**) and dibasal (**bb**) isomers generally interconvert only slowly in solution at room temperature on the NMR time scale, although inequivalent phosphorus centres in the apical-basal isomers interconvert rapidly at room temperature [**18**,**29**]. The room temperature $^{31}P\{^{1}H\}$ NMR spectrum of **1** in CD_2Cl_2 shows two sets of three resonances in an approximate 3:1 ratio assigned to isomers **1bba** and **1bbb**. The minor set, **1bbb**, are all sharp and consist of two doublets at 89.7 (J 17.2 Hz) and 61.6 ppm (J 9.2 Hz) and a doublet of doublets at 86.3 ppm. The major set, **1bba**, which are observed at 83.3, 81.8 and 63.9 ppm are all broad at this temperature and the individual coupling constants cannot be extracted. In each isomer, we assign the low-field resonances to the phosphorus bound to the iron dicarbonyl unit, the intermediate resonance to the central phosphorus atom of the triphos ligand and the high-field resonance to the chelate end of the tridentate phosphine. Upon warming a d^8-toluene solution of this mixture, there is no significant change in the ratio of **1bba**:**1bbb** and this suggests that the **bba** and **bbb** isomers do not interconvert readily, consistent with slow interconversion of apical-basal (**ab**) and dibasal (**bb**) coordination. Upon cooling a CD_2Cl_2 solution, resonances associated with **1bbb** do not vary significantly, however, those associated with **1bba** broaden and collapse until at 183 K they are replaced by twelve new, sharp resonances associated with four separate isomeric forms (labelled I to IV see experimental section for details).

We propose that the four isomers of **1bba** in the slow-exchange spectrum derive from conformational changes through; (i)“flipping” of the $Fe_2S_2C_3$ bridge across the Fe-Fe vector and

(ii) restricted motion of the phenyl rings and ethano-backbones associated with the triphos ligand. Scheme 3 shows the different ring-flip conformers (i.e., "flippamers") based on **1bba**, of which the structures of **bba (L)** and **bba (R)** [where the L (left) and R (right) designations refer to the flip orientation of the pdt ligand] were computationally optimised in order to explore the barrier for the flipping of the pdt ring in the structurally characterized form of this compound. Figure 3 shows the optimised structure of **1bba**, whose pdt ring adopts a distal orientation (left) with respect to the chelated iron center [i.e., the Fe(2) center in the solid-state structure of **1bba** shown in Figure 1). The species **bba (L)** in Scheme 3 corresponds to the DFT-optimised structure **A** depicted in Figure 3, while the pdt-flippamer is represented by **bba (R)** and whose optimised structure is species **B**. The energy difference (ΔG) between **A** and **B** favors the former species but only by 0.4 kcal/mol, rendering the two isomers isoenergetic for practical purposes. The computed barrier for pdt ring flipping in **A→B** is 9.7 kcal/mol (ΔG), and the process proceeds through a flattening of the carbocyclic ring of the pdt ligand, as verified by the optimised transition-state structure **TSAB**. Restricted motion of the phenyl rings and the ethano-backbones associated with the triphos ligand are likely responsible for the other pair of stereoisomers observed in the low-temperature NMR spectrum.

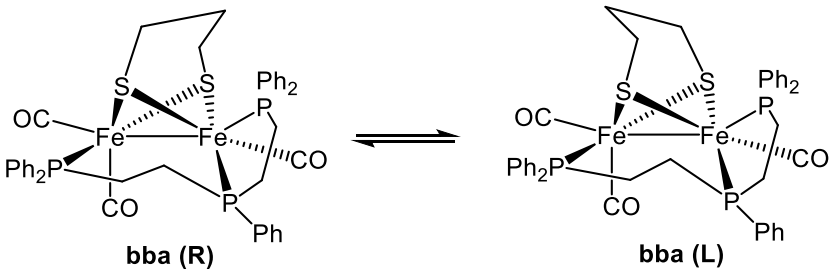

Scheme 3

In order to model the geometry of the **bbb** stereoisomer based on **1**, we employed structure **3** (Figure 2) and replaced the aza moiety with a methylene group. The optimised structure (species **C**) is fully consistent with this alternative stereoisomer. The pdt ring in **C** undergoes flipping to afford species **D** through **TSCD** in a process similar to that found for the conversion of the **A→B**.

While the interconversion of apical-basal sites of chelating diphosphine ligands (**ab** ⇌ **ba**) in $Fe_2(CO)_4(\kappa^2\text{-PP})(\mu\text{-SXS})$ derivatives is well-established and shown to proceed with low activation barriers [**18,29**], the constraints imposed by the triphos ligand retard this isomerisation

path within the chelate portion of the ligand. DFT calculations confirmed that the (**ab** ⇌ **ba**) isomerisation of the two phosphine ligands associated with the chelate ring in species **A**-**D** is energetically prohibitive. The effect of tripodal rotation of the CO and PPh_2 ligands about each iron center was also computationally examined for species **A** and **C**, but no stable structure could be found for the concerted rotation of the groups about the $Fe(CO)P_2$ moiety in either species. The $Fe(CO)_2P$ center is more flexible with respect to a tripodal rotation, and we were able to optimize an alternative structure where the PPh_2 moiety has exchanged sites with the equatorial CO group. Here species **A_Alt** and **C_Alt** were successfully optimised (Figure 5) and found to lie 12.8 and 13.0 kcal/mol higher in energy (ΔG), respectively, than their precursor. The unfavorable energy of **A_Alt** allows us to exclude it as a participant in the above VT NMR discussion. Attempts to extract the transition-state structure for the two tripodal rotations were unsuccessful.

Protonation studies - A key feature of iron-only hydrogenase models is their ability to bind a proton(s) [**40**-**48**]. Protonation rates are controlled electronically, being correlated with the energy of the metal-metal σ-bond (HOMO) which in turn is a function of the nature of the electron-donating ligands attached to the diiron centre [**48**]. Consequently, $Fe_2(CO)_3L_3$(μ-dithiolate) complexes are expected to protonate rapidly. Addition of *ca.* 1-2 equivalents of $HBF_4.Et_2O$ to a CH_2Cl_2 solution of **1** led, however, only to a slow change (over *ca.* 2 h) in the IR spectrum, but consistent with protonation at the diiron centre, initial carbonyl absorptions at 1947s and 1889vs cm^{-1} being replaced by new peaks at 2039vs, 1986s and 1964s cm^{-1} assigned to $[Fe_2(CO)_3(\mu\text{-pdt})(\mu,\kappa^1,\kappa^2\text{-triphos})(\mu\text{-H})][BF_4]$ (**1H**$^+$) (Scheme 4); the average blue shift of 88 cm^{-1} being consistent with protonation at the diiron centre. The salt was stable in air, and no further change was noted even after sitting for 3 d. In the $^{31}P\{^1H\}$ NMR spectrum a single set of three resonances was observed at 88.9, 85.2 and 46.4 ppm and upon cooling no significant changes were observed. In the ^1H NMR spectrum a doublet of triplets at δ −13.5 (J 29.2, 22.4 Hz) is assigned to the hydride resonance, both the position of couplings showing that it bridges the diiron centres. The large high-field shift (*ca.* 17.5 ppm) of the resonance associated with the chelate portion of the triphos ligand suggests that at least one of the PPh_2 moieties has been significantly perturbed, while in contrast, the other two phosphorus atoms change only slightly. Unfortunately, we have been unable to crystallographically characterise **1H**$^+$ but on the basis of spectroscopic measurements proposes that it adopts a **bbb** geometry (Scheme 4).

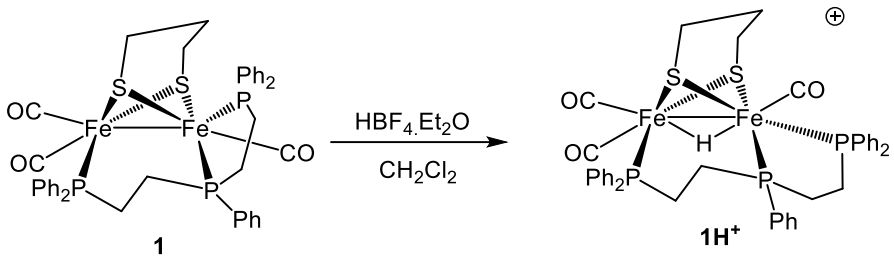

Scheme 4

Addition of two equivalents of $HBF_4{\cdot}Et_2O$ to CH_2Cl_2 solutions of **2** and **4** lead to similar observations, consistent with the slow protonation of the metal-metal bond; however, in both cases, the protonated product was considerably less stable than $\mathbf{1H^+}$. For **2**, new IR bands developed at 2043 and 1999 cm^{-1} being attributed to $\mathbf{2H^+}$. Attempts to isolate a pure product were unsuccessful and all samples were accompanied by significant decomposition. Similarly for **4**, generation of new bands at 2031, 2003 and 1964 cm^{-1} was consistent with the formation of $\mathbf{4H^+}$, but a pure sample could not be isolated.

The protonation behaviour of **3** was expectedly different given the presence of the basic aza-dithiolate moiety, which serves to direct protonation to the bridgehead nitrogen atom [**49-55**]. The neutral complex showed two carbonyl bands at 1951 and 1893 cm^{-1}, and on the addition of one equivalent of acid, these undergo a small shift and furnish three bands at 1970, 1922 and 1902 cm^{-1}. This is consistent with previous reports that protonation at the nitrogen in the bridge results in shifts of *ca*. 10-20 cm^{-1}, in contrast to *ca.* 60-100 cm^{-1} shift for protonation at the dimetal centre [**48,49**]. Addition of excess acid resulted in a further shift of the carbonyl stretching bands to 2097, 2051, 2022 and 1990 cm^{-1} indicative of protonation at the iron-iron bond. Thus it appears that $[Fe_2(CO)_3(\mu\text{-adtH})(\mu,\kappa^1,\kappa^2\text{-triphos})][BF_4]$ ($\mathbf{3H_N^+}$) initially results and that this is converted to doubly protonated $[Fe_2(CO)_3(\mu\text{-adtH})(\mu,\kappa^1,\kappa^2\text{-triphos})(\mu\text{-H})][BF_4]_2$ ($\mathbf{3H_2^{2+}}$) in the presence of excess acid (Scheme 5). Rauchfuss and co-workers have shown that the related tri-substituted complex $Fe_2(CO)_3(PMe_3)(\mu\text{-adt})(\kappa^2\text{-dppv})$ also first forms an ammonium cation, followed by the slow tautomerisation ($t_{1/2}$ = 30 min in CH_2Cl_2 room temperature) to the isomeric μ-hydride species [**14**]. Attempts to monitor the protonation of both **1** and **3** by ^1H NMR at low temperature were unsuccessful, signals simply broadening upon addition of acid which may result from concomitant oxidation of the diiron centre (see later).

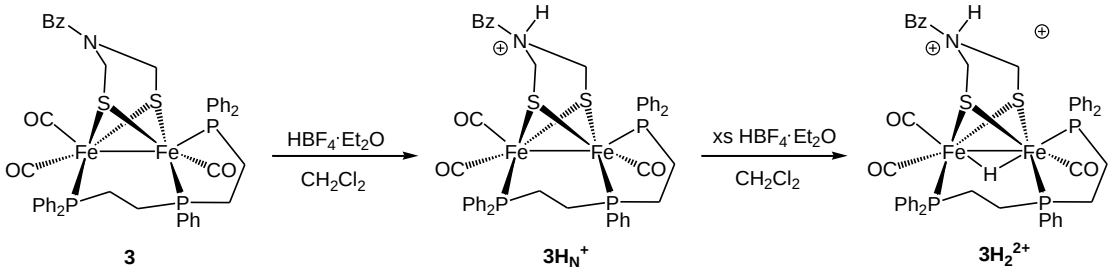

Scheme 5

The slow rate of protonation of **1** is unexpected. Pickett and co-workers [**48**] who have shown that the process is second order with the rate (k_H) showing a linear correlation with the energy of the HOMO, as measured by $E_{1/2}^{ox}$. On the basis of the measured $E_{1/2}^{ox}$ for **1** of -0.35 V (see below), an extrapolated rate of *ca.* 4500 $M^{-1}s^{-1}$ is expected. Clearly protonation of **1** and the other triphos complexes reported here must have a significant kinetic barrier, as rates (k_H) are nowhere near as high as predicted. Independent of the protonation kinetics, the final product **1H**$^+$ exhibits good thermodynamic stability. To better understand the slow protonation of **1** we considered the general protonation pathway as shown for disubstituted $Fe_2(CO)_4(\mu\text{-pdt})(PMe_3)_2$, whose reactivity has been thoroughly studied [**44**]. Thus with $[Et_2OH]^+$ (the acid used in this study), the initial formation of an intermediate in which this cation is bound to a terminal carbonyl is proposed, followed by rearrangement to give a terminal hydride, a transformation which also requires the development of a semi-bridging carbonyl. This species is unstable and converts to more stable bridging hydride isomers, the thermodynamically preferred species whose formation is accompanied by a significant rearrangement of the positions of the PMe_3 ligands (*via* Bailar twists) [**56**]. In mapping this general scheme onto the protonation of **1**, the formation of a carbonyl adduct should not be perturbed, but all other transformations are likely to be significantly changed. Thus the formation of the semi-bridging carbonyl is likely to be unfavourable at the sterically congested Fe_2(triphos) platform, while as shown above, movement of the triphos ligand between different coordination sites has much a higher energy barrier(s) than the movement of monodentate or bidentate phosphine ligands. We also note here that in the enzymes themselves it is terminal hydrides that are responsible for hydrogen production; the thermodynamically stable bridging hydride being off cycle [**1**], and its formation is prohibited by high activation barriers caused by interactions of the H-cluster with surrounding amino acids [**57**]. Thus, the kinetically slow protonation of **1H**$^+$ with a bridging hydride is not fully unexpected, and our triphos-tethered compounds function as outliers as compared to other tricarbonyl complexes, $Fe_2(CO)_3L_3(\mu\text{-}$

dithiolate), whose protonation is both kinetically and thermodynamically favoured. Unfortunately, we have been unable to identify any terminal hydride species in low-temperature protonation studies. The slow protonation of **1** is expected to have a significant effect on its behaviour as a proton reduction catalyst and, indeed, this has been experimentally established (see later).

Electrochemical studies – Figure 6a (brown trace) shows the CV of **1** in CH_2Cl_2/0.1 M $TBAPF_6$ (TBA = NBu_4). On sweeping first towards negative potentials, no reduction peak was observed within the available potential window, consistent with high electron-density at the diiron centre when ligated by three electron-donating phosphines. On scanning anodically, **1** undergoes oxidation at $E_{1/2}$ = -0.35 V (Table 1) in a process that was found to be reversible (i_p^{ox}/i_p^{red} *ca.* 1) over all scan rates studied (0.01 through 10 V s^{-1}) (see ESI). The stability of the oxidised $[FeFe]^+$ species allowed chronocoulometry experiments to be carried out, confirming unequivocally that the process was a one-electron transfer. Further irreversible anodic peaks were noted above 0.3 V, attributed to the $[FeFe]^{+/2+}$ process and oxidation of resulting products.

Table 1: Oxidation potentials for the first reversible oxidation of complexes **1**-**4** and $\mathbf{1H^+}$

Complex	**1**	**2**	**3**	**4**	$\mathbf{1H^+}$
$\mathbf{E_{1/2}}$ / V vs. Fc/Fc+	-0.35	-0.45	-0.35	-0.25	0.75

The edt complex **2** and unlinked **4** show similar electrochemical behaviour to **1**, but the oxidation potential is dependent on the identity of the bridging group, as summarised in Table 1. Complex **2** has $E_{1/2}$ = -0.45 V for the $[FeFe]^{0/+}$ couple, making it the most difficult of the four complexes to oxidise, while **4** was easier to oxidise than **1**, reversible oxidation taking place at $E_{1/2}$ = -0.25 V. A comparison of the relative oxidation peak currents for **1**, **2** and **4** allows the oxidation to be assigned as a one-electron process, i.e. $[FeFe]^{0/+}$ for all of the complexes. The electrochemical reversibility of the $[FeFe]^{0/+}$ process is unaffected by the bridging group, indicating little structural rearrangement on the timescale of electron transfer and hence a common mechanism for oxidation of these species. The difference in oxidation potentials is likely attributed to different frontier MO energies resulting from differing degrees of orbital overlap, dictated by the flexibility or constraint imposed by the bridging group.

The adt-complex **3** (Figure 6b) has quite different oxidation behaviour. Oxidation occurs reversibly at the same potential as for **1** ($E_{1/2}$ = -0.35 V), but a second oxidation couple of similar peak height is observed at $E_{1/2}$ = -0.11 V, suggestive of a further reversible one-electron oxidation. The scan rate dependence of the two couples (see ESI) shows the relative peak heights and separations of the two processes do not change significantly with scan rate. The behaviour observed may be attributed to the consecutive loss of two electrons from the same orbital; thus the first couple is assigned to the $[FeFe]^{0/+}$ process and the second to $[FeFe]^{+/2+}$. The ease of reversible oxidation of the $[FeFe]^{+}$ cation for **3** as compared to **1** is consistent with behaviour reported for $Fe_2(CO)_3(\mu\text{-adt})(\kappa^2\text{-dppv})(PMe_3)$ [**9**], which has been attributed to stabilisation of the $[FeFe]^{2+}$ dication by the nitrogen in the adt bridge. It was proposed that an iron-nitrogen bond is formed, resulting in stabilisation of the dication in the adt complex, while such an interaction between bridge and Fe centre is not possible for the pdt complex. No attempt was made to isolate dications.

We have also recorded the CV of $\mathbf{1H}^+$ in CH_2Cl_2/0.1 M $TBAPF_6$ (Figure 6a – black trace). Consistent with the removal of electron-density on the formation of the bridging hydride across the iron-iron bond, the first oxidation of the complex is shifted *ca*. 1.1 V towards more positive potentials ($E_{1/2}$ = 0.74 V) as compared to **1**. Unlike **1**, the first reduction of $\mathbf{1H}^+$ is observed within the potential window of the solvent, appearing as a quasi-reversible couple at $E_{1/2}$ = -1.7 V (i_p^{ox}/i_p^{red} = 0.65 at 0.1 V s^{-1}). Both oxidation and reduction of $\mathbf{1H}^+$ are one-electron processes, with the response being stable under repeated cycling. The stability of the reduced 35-electron species **1H** on the electrochemical time scale is consistent with voltammetry reported for some other bridging hydrides of phosphine substituted complexes [**40**,**58**].

Oxidation of hydrogenase biomimics usually results in a concomitant shift of a carbonyl from a terminal to semi-bridging site with the resultant twisting of the iron centres to a more staggered geometry [**5,6,59-61**]. In order to further probe the structure and the stability of the radical cation structures derived from **1**, we have carried out DFT calculations. The corresponding radical cations based on species **A** and **C** were successfully optimised, and the resulting structures are shown in Figure 7. Spin contamination in the radical cations is minimal, and $\mathbf{A_{ox}}$ lies 6.0 kcal/mol lower in energy than $\mathbf{C_{ox}}$. The flexibility of the triphos

ligand is assumed to be responsible for the computed energy difference, with the more flexible **bbb** isomer able to undergo partial tripodal reordering of the ancillary ligands at the $Fe(CO)_2P$ site to afford a semi-rotated structure in the gas phase. This partial tripodal rotation of these ligands allows one of the CO groups to adopt a semi-bridging interaction (2.858 Å) with the adjacent iron centre which helps to stabilize the cationic charge in the gas phase. Chemical oxidation of **1** was carried out *in situ* upon addition of one equivalent of $[Cp_2Fe][PF_6]$. The IR spectrum of the resulting complex $\mathbf{1}^+$ showed a single band at 1947 cm^{-1}, and we could find no evidence for a semi-bridging carbonyl as predicted by DFT. Repeating the optimization of $\mathbf{C_{ox}}$ in the presence of CH_2Cl_2 (implicit solvation) furnished a similar structure (not shown) that exhibited a significantly weaker semi-bridging CO interaction with the adjacent iron center (>3.00 Å) and confirmed the sensitive nature of the secondary semi-bridging CO interaction with the iron center. While $\mathbf{1}^+$ had some stability in solution, all attempts to isolate a pure sample resulted in slow decomposition.

*Electrocatalytic behaviour of **1** in the presence of $HBF_4{\cdot}EtO_2$* **-** Given that $\mathbf{1H}^+$ undergoes reversible oxidation at 0.75 V and reduction at -1.7 V, it is expected that addition of the strong acid $HBF_4{\cdot}Et_2O$ to **1** should result in redox features at these potentials. Broadly this is observed (Figure 8a), but protonation is not immediate, requiring the addition of 3–4 molar equivalents of acid before the oxidation couple of the neutral complex at -0.35 V disappears and is replaced with the reversible couple at 0.75 V assigned to oxidation of $\mathbf{1H}^+$. The relatively slow protonation of the highly basic **1** is consistent with earlier IR observations and suggests a significant kinetic barrier to protonation. Addition of up to five equivalents of acid results in increasing reduction currents at *ca*. -1.7 V, the potential at which $\mathbf{1H}^+$ undergoes reduction, suggesting proton reduction catalysis takes place at this potential (labelled **A** in Figure 8a). This pathway to hydrogen evolution is proposed to proceed *via* a CECE mechanism (**A**) as shown in Figure 8b. On addition of further acid equivalents, the catalytic current at this potential does not increase further but reaches a limiting value (see Figure 8 c). As the rate of this process rapidly becomes independent of proton concentration the rate-limiting step is likely H_2 elimination from **1(μH)H**, as has been described for $[Fe_2(CO)_4(\kappa^2\text{-dppe})(\mu\text{-pdt})(\mu\text{-H})]^+$ [**62**]. H_2 elimination first requires conversion of **1(μH)H** to **1-H₂** and given the rigidity and basicity of **1** this step is expected to be slow.

A further catalytic process (labelled **B**) is observed at *ca.* -2.1 V. Given that the **1(μH)H** species generated in process **A** is slow to eliminate H_2 on the electrochemical timescale, it is proposed that process **B** derives from the reduction of **1(μH)H** at *ca.* -2.1 V and its subsequent protonation, with hydrogen elimination taking place from resulting **1H(μH)H** (Figure 8b, **B**). Such a scenario has previously been described for catalysis involving $[Fe_2(CO)_4(\kappa^2\text{-dppe})(\mu\text{-pdt})(\mu\text{-H})]^+$, whereby the bridging hydride is proposed to behave as a spectator ligand [**61**]. This mechanism has been demonstrated experimentally for mixed-valence $[Fe_2(CO)_2(\kappa^2\text{-dppv})_2(\mu\text{-pdt})(\mu\text{-H})]^+$, where on addition of D^+ only D_2 was evolved, with no mixed DH product observed [**61**]. In the present study, we know that $\mathbf{1H^+}$ is thermodynamically stable (as it can be readily isolated), and as shown in Figure 6a, the complex **1H** generated during reduction of $\mathbf{1H^+}$ is stable towards electrochemical cycling. Thus the possibility of a catalytic cycle where **1H** acts as the catalyst, but the bridging hydride plays no role in the catalytic cycle is feasible. The mechanistic details of the further protonation of **1H** are yet to be elucidated, with the metal centres, bridging sulphur sites or the bridging hydride itself all being proposed in similar systems [**61,62**]. As shown in Figures 8a and 8c, process **B** reaches a limit after addition of about 5-6 acid equivalents, indicating that hydrogen elimination becomes rate limiting in this process also.

After addition of 4 equivalents of acid, a new process (labelled **C**) begins to grow in at *ca.* -1.6 V, some 100 mV positive of **A** (Figure 8a). This process has a non-linear relationship with $[H^+]$ and it appears to be related to the limiting of processes **A** and **B**, as it emerges at about the same acid concentration that they begin to reach their maximum rates (Figure 8c). We attribute these currents to the reduction of intermediates of the catalytic **A** and **B** cycles, which accumulate at the electrode interface during cycling. As H_2 elimination steps for **A** and **B** are rate-limiting, it follows that **1(μH)H** and **1H(μH)H** will build up in solution. Over the time scale of electrochemical cycling, they slowly release H_2, producing **1** and **1(μH)** respectively. Regeneration of **1** allows catalytic cycle **A** to proceed at -1.7 V. The fate of **1(μH)** is more complex, as at potentials above -1.7 V there is a competition between its oxidation to $\mathbf{1(\mu H)^+}$ (the reduction of $\mathbf{1H^+}$ was shown to be reversible in Figure 6 a) and further protonation to give $\mathbf{1(\mu H)H^+}$. Over time and in the presence of excess acid, increasing concentrations of $\mathbf{1(\mu H)H^+}$ are therefore likely to accumulate in solution, which we propose give rise to the reduction currents at -1.6 V.

*Effect of electrolyte composition on the electrocatalytic performance of **1*** - The catalytic performance of **1** and the relative contribution of peaks **A**, **B** and **C** to the total current was found to depend strongly on background electrolyte. Figure 9 shows how the limiting currents of processes **A**, **B** and **C** vary with concentration of HBF_4 in the presence of 0.1 M $TBAPF_6$, $TBABF_4$ and $TBAClO_4$. As described above, in $TBAPF_6$ process **A** reaches a maximum rate after addition of only 4 equivalents of acid. In contrast, in $TBAClO_4$ the limiting current increases linearly with acid concentration up to the addition of 10 equivalents. In $TBABF_4$ the behaviour is intermediate, with the rate of catalysis slowing after addition of 5 equivalents, but without reaching a limiting value as observed in $TBAPF_6$. These observations suggest that the anion plays a significant role in key steps of catalytic mechanism **A**, with the rate increasing in the order $PF_6^- < BF_4^- < ClO_4^-$.

Process **B** competes with **A** and hence its rate depends on the ease of H_2 elimination from **1(μH)H** in pathway **A**. This is reflected in the limiting currents for **B** on addition of 1-5 equivalents of acid, where the currents in the presence of PF_6^- are marginally higher than those in BF_4^- which are higher than those in ClO_4^- (Figure 9). This is consistent with more **1(μH)H** being available for reduction at -2.1 V in PF_6^- as H_2 elimination is so slow under these conditions. Conversely, in the presence of ClO_4^- where the larger currents for process **A** suggest that H_2 elimination from **1(μH)H** is faster, currents due to **B** are initially the smallest as there will be less **1(μH)H** available at the electrode interface to partake in the reaction. With the addition of further acid, process **B** begins to reach a constant rate in PF_6^-, suggesting that H_2 elimination (this time from **1H(μH)H**) is rate-limiting. This is not the case for BF_4^- and ClO_4^-, where currents continue to increase with acid addition, indicating H_2 elimination steps are faster in the presence of these anions.

Process **C** has a similar, but more complex, acid dependence in all three electrolytes. In all cases, currents at potential **C** only emerge after addition of 4-5 acid equivalents and thereafter increase in a non-linear fashion. As described above, process **C** is attributed to the reduction of **1(μH)H**$^+$, which accumulates at the electrode surface over time, due to slow H_2 elimination from **1H(μH)H** and subsequent protonation of **1(μH)**. The currents for this process are greatest in the presence of ClO_4^- as H_2 elimination is fastest under these conditions, allowing higher concentrations of **1(μH)H**$^+$ to build up over time.

The role of anions in protonation and hydrogenation equilibria of metal hydrides has been reported previously, for complexes such as $[FeH(\kappa^2\text{-}H_2)(\kappa^2\text{-dppe})_2]^+$ [**63**] and $[W_3(\mu_3\text{-}S)(\mu\text{-}S)_3H_3(\kappa^2\text{dmpe})_3]^+$ [**64**] as well as $Fe_2(CO)_2(\kappa^2\text{-dppv})_2(\mu\text{-adt})$ [**65**]. In these studies it was proposed that ion pairs form between the metal complex and the anion and this lowers activation barriers for intramolecular proton transfer from one site to another. Our results suggest that the anion may play a role in the hydrogen elimination step. As indicated in Figure 8b, this requires the combination of two protons bound at different sites on the molecule (e.g. to form **1-H$_2$** from **1(μH)H** or **1(μH)-H$_2$** from **1H(μH)H**) and we suggest that the shuttling of H from one site on the molecule to another may be facilitated by ion pairing to BF_4^- or ClO_4^-, hence catalysis is more efficient in the presence of these ions. Ion pairing with PF_6^- may not be possible for steric or other reasons. Different solvents have also been shown to influence protonation sites and equilibria [**66**], so it is also possible that the $TBAPF_6$, $TBABF_4$ and $TBAClO_4$ salts used in this study had varying water content, and the presence of trace water may also influence site and rate of proton transfer. Due to the low synthetic yield we were unable to test the electrocatalytic behaviour of **2**, however **4** exhibited broadly similar trends to **1** (see ESI).

*Electrocatalytic behaviour of **3** on the addition of strong acid* – The behaviour of **3** on addition of $HBF_4{\cdot}Et_2O$ in the presence of $TBAPF_6$ is very different to that observed for **1** (Figure 10a). Addition of one acid equivalent results in the immediate loss of the oxidation peaks for **3** at -0.35 and -0.11 V and the appearance of a new oxidation peak at 0.15 V vs. Fc/Fc^+. The shift of oxidation potential by +0.5 V in the presence of acid is consistent with protonation of the adt-bridge [**49**]. Thus, a shift of *ca.* +1.1 V is anticipated for protonation at iron, but for **3** we observe no clear evidence of an oxidation peak at 0.75 V, suggesting that protonation has taken place solely at the adt nitrogen. Addition of one equivalent of acid also results in the emergence of a broad reduction peak at *ca.* -1.9 V (**D**), attributed to the reduction of **3H$_N^+$**. This increases with the addition of up to 3-4 acid equivalents, indicating H^+ reduction catalysis at this potential. A possible CECE mechanism for the processes contributing to **D** is shown in Figure 10c; after reduction of **3H$_N^+$** at -1.9 V, protonation of **3H$_N$** at the iron-iron bond is proposed, resulting in **3H$_N$H$_{Fe}^+$**. As one would expect a species protonated at iron to be reduced more readily than **3H$_N^+$** (as electron density has been removed from the iron centre) **3H$_N$H$_{Fe}^+$** is likey to undergo rapid reduction at this potential to give **3H$_N$H$_{Fe}$**. The final step of H_2 elimination is rate-limiting and slow, as the catalytic

process becomes independent of acid concentration after addition of 3 acid equivalents. A further reduction process is noted at *ca*. -2.1 V, l due to the reduction of $\mathbf{3H_NH_{Fe}}$, but this appears not to be catalytic. Marked on Figure 10a is the position of process **A** observed for **1**, associated with species protonated at the Fe-Fe bond. For **3** no significant increase in current is noted at these potentials, which suggests protonation at iron does not compete effectively with protonation at nitrogen under these conditions.

In contrast, as shown in Figure 10b, the addition of excess acid to **3** in $TBABF_4$ (green trace) and $TBAClO_4$ (orange trace) electrolytes results in increased reduction currents at *ca*. -1.6 V (**E** and **F**) at similar potentials to processes **A** and **C** observed for **1**, suggesting the involvement of species protonated at the iron-iron bond. This is consistent with IR observations of the shift of CO bands to higher wavenumber on addition of excess acid to **3**. The reduction potential for these species is electrolyte-dependent and there is little reduction observed at this potential in $TBAPF_6$ (brown). A speculative mechanism for this catalytic process is shown in Figure 10c. We propose that in excess acid $\mathbf{3H_N^+}$ undergoes further protonation to give $\mathbf{3H_NH_{Fe}^{2+}}$ and the reduction of this species gives rise to currents observed at **E** and **F** in Figure 10b. Hydrogen-elimination is again the rate limiting step in the process, resulting in slow regeneration of **3**. The similar dependency of the rate of this process on electrolyte anion identity is consistent with the results observed for **1** and further suggests the anion plays a role in the H_2 elimination step.

SUMMARY AND CONCLUSIONS

Introduction of the triphos ligand into hydrogenase biomimics allows access to complexes **1-4** containing the biologically relevant $Fe_2(CO)_3L_3$(μ-dithiolate) framework. In contrast to other complexes of this type, which rely on separate addition of monodentate and bidentate ligands [**3-16**], triphos complexes represent a new class of biomimics in which all three substituted ligands are conjoined and this imposes some structural rigidity upon the molecule as well as sterically inhibiting access to the central iron-iron bond. Structural and spectroscopic studies show that a range of isomers are possible. An important finding is that although the diiron centre is basic, protonation is slow; likely a result of the relative inaccessibility of a protonation site. This is supported by computational work by De Gioia and co-workers who investigated

factors affecting the kinetics and thermodynamics of protonation of $Fe_2(CO)_3(\mu\text{-edt})(PMe_3)(\kappa^2\text{-dppv})$ [**8**]; the presence of the bulky ligands significantly affecting the rate of protonation. Although protonation of **1** affords the thermodynamically favoured bridging hydride, $\mathbf{1H^+}$, which likely proceeds via initial formation of a terminal hydride, De Gioia's work suggesting that the most stable terminal hydride is that bound to the least-substituted iron centre [**8**]. In $Fe_2(CO)_3(\mu\text{-edt})(PMe_3)(\kappa^2\text{-dppv})$ formation of this terminal hydride led to a trigonal rotation of this iron centre with formation of a bridging carbonyl ligand, a situation also seen in the well-studied tetra-substituted model complexes $Fe_2(CO)_2(\kappa^2\text{-dppv})_2(\mu\text{-dithiolate})$ [**65-69**] and $Fe_2(CO)_2(PMe_3)_4(\mu\text{-dithiolate})$ [**70**]. We suggest that for **1-4** this is a high energy process and thus renders formation of such a species unfavourable. With regards to the hydrogenase enzyme, the active site is constrained within a protein structure, where secondary interactions impose restrictions on the flexibility of the H-cluster and access to the Fe-Fe bond. In particular, the formation of a bridging hydride species is prevented, as access to the bond is blocked.

Given the slow rate of protonation of **1-4** it might be expected that this would be rate-limiting in catalytic proton-reduction. However, it was found that for **1** and **3-4**, H_2 elimination is slow and moreover their rates are highly dependent on electrolyte composition. For **1** and **4** the key steps that are influenced by the identity of electrolyte anion seem to be combining of two hydrides and their elimination as H_2. These steps, involving proton-transfer from one site to another, are facilitated by ions such as BF_4^- and ClO_4^- that can effectively form ion pairs with the complex [**15**]. The larger, bulkier PF_6^- ion does not effectively aid this H transfer process, and for the $(\mu\text{-SMe})_2$ complex **4** showed evidence of inhibiting electrocatalysis altogether, suggesting it may even block key sites. The slow rate of the H_2 elimination may be attributed partly to the thermodynamic stability of the intermediate bridging hydride species. This is illustrated by the ease of isolation of $\mathbf{1(\mu H)^+}$ and ability to reversibly cycle this molecule through the $1^-/0/1^+$ oxidation states; thus **1(μH)** is very stable, and even on further protonation and reduction the bridging hydride has a high tendency to remain intact. In addition, the second proton may bind at a site removed from the bridging hydride, due to the presence of the relatively bulky triphos ligand. This site could be a terminal hydride on one of the iron centres or the sulphur of the bridging group. The rigidity of the complex imposes a large barrier to the intramolecular proton transfer and its combination with the bridging hydride; hence this step is very likely to be slow. For the adt complex we observe that the

triphos ligand imposes similar constraints on protonation at the Fe-Fe bond, with protonation at adt preferred. Again, the presence of BF_4^- or ClO_4^- (but not PF_6^-) apparently facilitates H_2 elimination from **3H$_N$H$_{Fe}$**, emphasising the role of effective intramolecular proton transfer in the maintenance of a catalytic cycle.

EXPERIMENTAL SECTION

General Procedures and Starting Materials. Unless otherwise noted, all the reactions were carried out under a nitrogen atmosphere using standard Schlenk techniques. Reagent-grade solvents were dried using appropriate drying agents and distilled prior to use by standard methods. Infrared spectra were recorded on a Nicolet 6700 FT-IR spectrometer in a solution cell fitted with calcium fluoride plates, subtraction of the solvent absorptions being achieved by computation. NMR spectra were run on a Bruker AMX400 instrument. Mass spectra were recorded on a Varian Mat 312 mass spectrometer. Elemental analyses were performed by Microanalytical Laboratories, University College London. Collman's reagent and PPh_3 were purchased from Strem Chemical Inc. and used without further purification.

Preparation of $Fe_2(CO)_3(\mu\text{-pdt})(\mu,\kappa^1,\kappa^2\text{-triphos})$ (1). A toluene solution (50 mL) of triphos (0.267 g, 0.05 mmol) and $Fe_2(CO)_6(\mu\text{-pdt})$ (0.221 g, 0.067 mmol) [**71**] was heated at reflux for 16 h. Upon cooling to room temperature the solvent was removed *in vacuo* and the residue washed with hexane to remove unreacted starting materials. Chromatography on alumina eluting with light petroleum-diethyl ether (1:1) gave a faint yellow band which was discarded. Eluting with dichloromethane gave a large red band which afforded a red-brown solid identified as $Fe_2(CO)_3(\mu\text{-pdt})(\mu,\kappa^1,\kappa^2\text{-triphos})$ (**1**) (0.387 g, 93 %). A second dark red band eluted upon addition of a small amount of methanol but this product was not characterised. Recrystallization of **1** from the slow mixing of methanol with a concentrated CH_2Cl_2 solution afforded crystals suitable for crystallography. IR ν(CO)(CH_2Cl_2): 1947s, 1889vs cm^{-1}; ^{1}H NMR (CD_2Cl_2, 298 K): δ 8.03 – 7.16 (m, 25H, Ph), 3.04 – 2.41 (m, 8H, PCH_2), 2.36 (br, 2H, SCH_2), 2.29 (br, 2H, SCH_2), 2.14 (br, 2H, CH_2); $^{31}P\{^1H\}$ NMR (CD_2Cl_2, 298 K): δ 89.7 (d, J 17.2, **1bbb**), 86.3 (dd, J 17.2, 9.2, **1bbb**), 83.3 (br, **1bba**), 81.8 (brd, J 23.4, **1bba**), 63.9 (br, **1bba**), 61.6 (d, J 9.2, **1bbb**) ratio **1abb**:**1bbb** *ca.* 7:3; (183 K) δ 91.74 (d, J 29.1, **1bba**^{I}), 88.34 (d, J 28.1, **1bba**^{II}), 87.78 (d, J 16.3, **1bbb**), 86.11 (dd, J 16.3, 9.2, **1bbb**), 83.52 (dd, 27.7, 9.4, **1bba**^{I}), 80.70 (dd, m, **1bba**$^{II+III}$), 77.48 (d, J 25.0, **1bba**^{III}), 76.90 (dd, J 25.3, 6.5,

1bba^{IV}), 74.42 (d, J 6.6, **1bba**^{IV}), 71.99 (d, J 6.0, **1bba**^{III}), 70.64 (d, J 25.0, **1bba**^{IV}), 64.88 (d, J 9.2, **1bbb**), 61.44 (d, J 9.8, **1bba**^{II}), 57.66 (d, J 9.8, **1bba**^{I}), ratio **1bbb**:**1abba**^{I}:**1bba**^{II}:**1bba**^{III}:**1bba**^{IV} *ca* 1:1:0.7:0.3:0.5; Anal. calc. for $Fe_2P_3S_2O_3C_{40}H_{39}$: C, 57.42, H, 4.67; Found C, 57.54, H, 3.86.

Preparation of $Fe_2(CO)_3(\mu\text{-edt})(\mu,\kappa^1,\kappa^2\text{-triphos})$ (2). A toluene solution (50 mL) of triphos (0.077 g, 0.014 mmol) and $Fe_2(CO)_6(\mu\text{-edt})$ (0.0.60 g, 0.016 mmol) [**70**] was heated at reflux for 16 h. Upon cooling to room temperature, the solvent was removed *in vacuo* and the residue washed with hexane to remove unreacted starting materials. A $^{31}P\{^1H\}$ NMR spectrum of the crude reaction mixture revealed a very complex mixture of products. Chromatography on alumina afforded a large number of bands which could not be fully separated. The crude reaction mixture (from a second reaction) was then again washed with hexanes and dried. The whole mixture was then dissolved in a minimum volume of dichloromethane and this was layered with approximately twice the volume of methanol. After mixing a brown solid was produced and this contained a small number of well-formed large crystalline blocks of $Fe_2(CO)_3(\mu\text{-edt})(\mu,\kappa^1,\kappa^2\text{-triphos})$ (**2**). These were used for crystallographic and analytical characterization. The brown solid was found to be impure **2** and a second batch of pure **2** was produced upon repeating the crystallization procedure. The overall yield of **2** is difficult to estimate but *ca.* 15 mg (13 %) of pure material was isolated. IR $\nu(CO)(CH_2Cl_2)$: 1951s, 1902vs cm^{-1}; ^1H NMR (CD_2Cl_2, 298 K): δ 7.87 – 7.08 (m, 25H, Ph), 3.43 – 1.27 (m, 12H, PCH_2 + SCH_2), $^{31}P\{^1H\}$ NMR (CD_2Cl_2, 298 K): δ 93.9 (d, J 13.9, **2bbb**), 87.3 (d, J 26.5, **2abb**), 86.9 (dd, J 13.9, 8.9, **2bbb**), 84.7 (d, J 26.5, **2abb**), 68.6 (s, **2abb**), 65.8 (d, J 8.9, **2bbb**) ratio **2abb**:**2bbb** *ca* 3:7; Anal. calc. for $Fe_2P_3S_2O_3C_{39}H_{37}$: C, 56.93, H, 4.50; Found C, 57.06, H, 4.66.

Preparation of $Fe_2(CO)_3(\mu\text{-adt})(\mu,\kappa^1,\kappa^2\text{-triphos})$ (3). A toluene solution (50 mL) of triphos (0.237 g, 0.044 mmol) and $Fe_2(CO)_6(\mu\text{-adt})$ (0.200 g, 0.049 mmol) [**72**] was heated at reflux for 19 h. Upon cooling to room temperature the solvent was removed *in vacuo* and the residue washed with hexane to remove unreacted starting materials. The dry solid was dissolved in a minimum volume of dichloromethane and an excess of hexane was added resulting in precipitation of a red solid identified as $Fe_2(CO)_3(\mu\text{-adt})(\mu,\kappa^1,\kappa^2\text{-triphos})$ (**3**) (0.379 g, 94 %). Crystallization of **3** from the slow mixing of methanol with a concentrated CH_2Cl_2 solution afforded crystals suitable for crystallography. IR $\nu(CO)(CH_2Cl_2)$: 1952s, 1895vs cm^{-1};

^{1}H NMR (CD_2Cl_2, 308 K)**:** δ 8.25 – 7.15 (m, 30H, Ph), 4.40 – 1.90 (brm, 14H, CH_2); $^{31}P\{^{1}H\}$ NMR (CD_2Cl_2, 308 K): δ 89.4 (br, **3bbb**), 84.9 (br, **3bbb**), 81.4 (br, **3abb**), 80.9 (br, **3abb**), 65.3 (br, **3abb**), 62.5 (br, **3bbb**) ratio **3abb**:**3bbb** *ca* 4:1; (223 K) δ 91.4 (br, **3abb**), 88.57 (d, J 13.0, **3bbb**), 88.3 (s, **3abb**), 84.9 (s, **3bbb**), 82.9 (br, **3abb**), 81.8 (br, **3abb**), 78.1 (br, **3abb**), 76.3 (s, **3abb**), 74.1 (s, **3abb**), 71.0 (s, **3abb**), 64.63 (s, **3bbb**), 61.5 (s, **3abb**), 57.2 (br, **3abb**); Anal. calc. for $Fe_2P_3S_2O_3N_1C_{46}H_{44}$: C, 59.54, H, 4.75; Found C, 59.74, H, 4.88.

Preparation of $Fe_2(CO)_3(\mu\text{-}SMe)_2(\mu,\kappa^1,\kappa^2\text{-triphos})$ (4). A toluene solution (50 mL) of triphos (0.100 g, 0.019 mmol) and $Fe_2(CO)_6(\mu\text{-}SMe)_2$ (0.100 g, 0.027 mmol) [**73**] was heated at reflux for 16 h. Upon cooling to room temperature, the solvent was removed *in vacuo* and the residue washed with hexane to remove unreacted starting materials. The dry solid was dissolved in a minimum volume of dichloromethane and an excess of hexane was added resulting in precipitation of a red solid identified as $Fe_2(CO)_3(\mu\text{-}SMe)_2(\mu,\kappa^1,\kappa^2\text{-triphos})$ (**4**) (0.094 g, 61 %). IR ν(CO) (CH_2Cl_2): 1952s, 1895vs cm^{-1}; ^{1}H NMR ($CDCl_3$, 253 K)**:** δ 7.95 – 7.12 (m, 25H, Ph), 3.40 – 1.50 (m, 8H, PCH_2), 1.25 (s, 3H, Me), 0.87 (s, 3H, Me); $^{31}P\{^{1}H\}$ NMR ($CDCl_3$, 253 K): δ 88.9 (d, J 19.4), 81.9 (dd, J 19.4, 9.7), 62.5 (d, J 9.7); Anal. calc. for $Fe_2P_3S_2O_3C_{39}H_{39}$: C, 56.79, H, 4.73; Found C, 56.35, H, 4.86**.**

Preparation of $[Fe_2(CO)_3(\mu\text{-}pdt)(\mu,\kappa^1,\kappa^2\text{-triphos})(\mu\text{-}H)][BF_4]$ ($1H^+$). A red CH_2Cl_2 solution (*ca.* 5 mL) of **1** (20 mg) turned cloudy and pink upon addition of a slight excess of $HBF_4.Et_2O$. IR studies showed the clean generation of new carbonyl bands consistent with the consumption of **1.** The mixture was stirred for 30 mins and the solvent was removed under reduced pressure to give an oil which was washed with diethyl ether (2 x 1 ml) and dried to give $[Fe_2(CO)_3(\mu\text{-}pdt)(\mu,\kappa^1,\kappa^2\text{-triphos})(\mu\text{-}H)][BF_4]$ (**1H**$^+$) as a dry pink solid (12 mg, 55%). IR ν(CO)(CH_2Cl_2): 2039vs, 1986s, 1964s cm^{-1}; ^{1}H NMR (CD_2Cl_2)**:** δ 7.80–7.32 (m, 25H, Ph), 3.55 – 1.62 (m, 14H, CH_2), -13.5 (dt, 1H, J 29.2, 22.4 Hz); $^{31}P\{^{1}H\}$ NMR (CD_2Cl_2) 88.9 (s), 85.2(s), 46.4 (s) ppm.

IR protonation studies on 1-4. CH_2Cl_2 solutions (*ca.* 1 mL) of **1-4** were prepared by dissolving 2.5×10^{-3} mmol of the complex and two molar equivalent amount of $HBF_4{\cdot}Et_2O$ (0.680 μL) was added to each. The resultant acid-containing solution was immediately transferred to an IR cell and monitored over time. For **1** no discernible change in the IR spectrum was noted after 30 mins. After 2 h the formation of small amounts of **1H**$^+$ was

noted. For **2** a slow (*ca.* 1 h) lightening of the red solution lead to the generation of new IR bands at 2043vs and 1999s cm^{-1} but over this time there was also substantial decomposition. For **3** a rapid (*ca.* 1 min) lightening of the solution occurred, and new IR bands were observed at 2042vs, 2021m and 1988m cm^{-1}. This species also decomposed slowly and all attempts to further characterize the product were unsuccessful. Addition of excess acid resulted in the formation of new IR bands at 2097w, 2051vs, 2033s and 1990s cm^{-1}. For **4** the dark red solution lighted slowly and new IR bands at 2031s, 2003s and 1964vs cm^{-1} appeared alongside those of **4**. These ν(CO) bands slowly decayed with the concomitant decomposition of the product over ca. 3 h.

Chemical oxidation of 1. $[Cp_2Fe][PF_6]$ (0.828 mg, 2.5×10^{-3} mmol) was dissolved in a minimum amount of CH_2Cl_2 and this solution was then added to a CH_2Cl_2 solution containing 2.5×10^{-3} mmol of **1** in CH_2Cl_2. The mixture was immediately transferred to an IR cell and monitored over time. IR absorptions for **1** were immediately replaced by a new strong absorption at 1947 cm^{-1} which is attributed to the formation of $[Fe_2(CO)_3(\mu\text{-pdt})(\mu,\kappa^1,\kappa^2\text{-triphos})][PF_6]$ (**1**$^+$).

Electrochemistry. Electrochemistry was carried out in deoxygenated dichloromethane with 0.1 M $TBAPF_6$ as supporting electrolyte. The working electrode was a 3 mm diameter glassy carbon electrode which was polished with 0.3 μm alumina slurry prior to each scan. The counter electrode was a Pt wire and the quasi-reference electrode was a silver wire. All CVs were referenced to the Fc^+/Fc redox couple. An Autolab potentiostat (EcoChemie, Netherlands) was used for all electrochemical measurements. Catalysis studies were carried out by adding equivalents of $HBF_4{\cdot}Et_2O$ (Sigma-Aldrich).

X-ray crystallography. Single crystals were mounted on fibres and diffraction data collected at 150 K on a Bruker SMART APEX diffractometer using Mo-Kα radiation (λ = 0.71073 Å). Data collection, indexing and initial cell refinements were all done using SMART software [**74**]. Data reduction was accomplished with SAINT [**75**] software and SADABS [**76**] programs were used to apply empirical absorption corrections. The structures were solved by direct methods or Patterson methods and refined by full matrix least-squares (SHELXTL, V6.12) [**77**]. All non-hydrogen atoms were refined anisotropically and hydrogen atoms were

included using a riding model. Scattering factors were taken from International Tables for X-ray Crystallography. Details of data collection and structure refinement are given in Table 2.

Computational methodology. The DFT calculations reported here were performed with the Gaussian 09 package of programs [**78**]. The calculations were carried out with the B3LYP functional, which utilizes the Becke three-parameter exchange functional (B3) [**79**] combined with the correlation functional of Lee, Yang, and Parr (LYP) [**80**]. The iron atoms were described by Stuttgart-Dresden effective core potentials (ecp) and SDD basis set, while the 6-31G(d') basis set was employed for the remaining atoms. The geometry-optimised structures reported here represent minima based on zero imaginary frequencies (positive eigenvalues) or as transition states with one negative eigenvalue, as established by frequency calculations using the analytical Hessian. Unscaled vibrational frequencies were used to make zero-point and thermal corrections to the electronic energies. The geometry-optimised structures have been drawn with the *JIMP*2 molecular visualization and manipulation program [**81**].

ASSOCIATED CONTENT

Text, tables and cif files giving details of the X-ray crystallographic structure determinations of **1** and **3** are available free of charge at http://pubs.acs.org or http://www.ccdc.cam.ac.uk/conts/retrieving.html as supplementary publications: CCDC Nos. 61463812 and 1897288 Union Road, Cambridge, CB2 1FZ, U.K.: fax: +44-1223-336033; e-mail: deposit@ccdc.cam.ac.uk). Atomic coordinates and energies of all optimised stationary points available. Some additional electrochemical information (Figures ES1-S5) and experiments, crystallographic data and computational details are given in electronic supplementary information.

AUTHOR INFORMATION

Corresponding Authors

Email: Graeme Hogarth (graeme.hogarth@kcl.ac.uk); Katherine Holt (k.b.holt@ucl.ac.uk)

Notes.

The authors declare no competing financial interests.

ACKNOWLEDGEMENTS

We thank University College London for the provision of a studentship (DU), the EPSRC for an Advanced Fellowship (KBH Grant No EP/D070538/1), the Commonwealth Scholarship Commission (SG) and Professors Phillip Schollhamer and Jean Talarmin for hosting DU in Brest enabling preliminary electrochemical measurements. GH thanks The Royal Society of Chemistry for an International Authors Grant which allowed this work to be developed during his visit to the University of North Texas and King's College London for funding. MGR acknowledges financial support from the Robert A. Welch Foundation (Grant B-1093-MGR). Computational resources through the High-Performance Computing Services and CASCaM at the University of North Texas are acknowledged, and we thank Prof. Michael B. Hall (Texas A&M University) for providing us a copy of his *JIMP2* program, which was used to prepare the geometry-optimised structures reported here.

REFERENCES

1 For reviews, see for example: (a) D. Schilter, J.M. Camara, M.T. Huynh, S. Hammes-Schiffer and T.B. Rauchfuss, *Chem. Rev*., 2016, **116**, 8693-8749. (b) W. Lubitz, H. Ogata, O. Rüdiger and E. Reijerse, *Chem. Rev.*, 2014, **114**, 4081–4148. (c) T. R. Simmons, G. Berggren, M. Bacchi, M. Fontecave and V. Artero, *Coord. Chem. Rev.*, 2014, **270–271**, 127–150.

2 For reviews, see for example: (a) I.P. Georgakaki, L.M. Thomson, E.J. Lyon, M.B. Hall and M.Y. Darensbourg, *Coord. Chem. Rev*., 2003, **238-239**, 255-266. (b) D.J. Evans, C.J. Pickett, *Chem. Soc. Rev*., 2003, **32**, 268-275. (c) L. Sun, B. Åkermark and S. Ott, *Coord. Chem. Rev*., 2005, **249**, 1653-6663. (d) X. Liu, S.K. Ibrahim, C. Tard and C.J. Pickett, *Coord. Chem. Rev*., 2005, **249**, 1641-1652. (e) J.-F. Capon, F. Gloaguen, F.Y. Pétillon, P. Schollhammer and J. Talarmin, *Coord. Chem. Rev*., 2005, **249**, 1664-1676. (f) C. Tard and C.J. Pickett, Chem. Rev., 2009, **109**, 2245-2274. (g) J.-F. Capon, F. Gloaguen, F.Y. Pétillon, P. Schollhammer and J. Talarmin, *Coord. Chem. Rev*., 2009, **253**, 1476-1494. (h) N. Wang, M. Wang and L. Chen, L. Sun, *Dalton Trans*., 2013, **42**, 12059-12071. (i) S. Tschierlei, S. Ott and R. Lomoth, *Energy Env. Sci.*, 2011, **4**, 2340-2352.

3 J.I. van der Vlugt, T.B. Rauchfuss and S.R. Wilson, *Chem. Eur. J.*, 2006, **12**, 90-98.

4 D. Chouffai, G. Zampella, J.-F. Capon, L. De Gioia, A. Le Goff, F.Y. Pétillon, P. Schollhammer and J. Talarmin, *Organometallics*, 2012, **31**, 1082-1091.

5 A.K. Justice, T.B. Rauchfuss and S.R. Wilson, *Angew. Chem., Int. Ed.*, 2007, **46**, 6152-6154.

6 A.K. Justice, L. De Gioia, M.J. Nilges, T.B. Rauchfuss, S.R. Wilson and G. Zampella, *Inorg. Chem.*, 2008, **47**, 7405-7414.

7 M.T. Olsen, B.E. Barton and T.B. Rauchfuss, *Inorg. Chem.*, 2009, **48**, 7507-7509.

8 G. Zampella, P. Fantucci and L. De Gioia, *J. Am. Chem. Soc*., 2009, **131**, 10909-10917.

9 M.T. Olsen, T.B. Rauchfuss and S.R. Wilson, *J. Am. Chem. Soc*., 2010, **132**, 17733-17740.

10 J.M. Camara and T.B. Rauchfuss, *J. Am. Chem. Soc*., 2011, **133**, 8098-8101.

11 A. Silakov, M.T. Olsen, S. Sproules, E.J. Reijerse, T.B. Rauchfuss and W. Lubitz, *Inorg. Chem*., 2012, **51**, 8617-8628.

12 J.M. Camara and T.B. Rauchfuss, *Nat. Chem*., 2012, **4**, 26-30.

13 J.C. Lansing, J.M. Camara, D.E. Gray and T.B. Rauchfuss, *Organometallics*, 2014, **33**, 5897-5906.

14 B.E. Barton, M.T. Olsen and T.B. Rauchfuss, *J. Am. Chem. Soc*., 2008, **130**, 16834-16835.

15 P.-Y. Orain, J.-F. Capon, F. Gloaguen, F.Y. Pétillon, P. Schollhammer, J. Talarmin, G. Zampella, L. De Gioia and T. Roisnel, *Inorg. Chem.*, 2010, **49**, 5003-5008.

16 D. Chouffai, G. Zampella, J.-F. Capon, L. De Gioia, F. Gloaguen, F.Y. Pétillon, P. Schollhammer and J. Talarmin, *Inorg. Chem*., 2011, **50**, 12575-12585.

17 J.-F. Capon, F. Gloaguen, F. Y. Pétillon, P. Schollhammer and J. Talarmin, *Eur. J. Inorg. Chem*., 2008, 4671-4681.

18 S. Ezzaher, J.-F. Capon, F. Gloaguen, F. Y. Pétillon, P. Schollhammer and J. Talarmin, *Inorg. Chem*., 2007, **46**, 3426-3428.

19 S. Ezzaher, J.-F. Capon, F. Gloaguen, F. Y. Pétillon, P. Schollhammer and J. Talarmin, *Inorg. Chem*., 2007, **46**, 9863-9872.

20 S. Ezzaher, J.-F. Capon, F. Gloaguen, N. Kervarec, F. Y. Pétillon, R. Pichon, P. Schollhammer and J. Talarmin, *C. R. Chim*., 2008, **11**, 906-914.

21 S. Ezzaher, J. -F. Capon, F. Gloaguen, F. Y. Pétillon, P. Schollhammer, J. Talarmin and N. Kervarec, *Inorg. Chem.*, 2009, **48**, 48, 2-4.

22 S. Lounissi, J.-F. Capon, F. Gloaguen, F. Matoussi, F. Y. Pétillon, P. Schollhammer and J. Talarmin, *Chem. Commun*., 2011, **47**, 878-880.

23 D. Chouffai, G. Zampella, J.-F. Capon, L. De Gioia, A. Le Goff, F. Y. Pétillon, P. Schollhammer and J. Talarmin, *Organometallics*, 2012, **31**, 1082-1091.

24 S. Lounissi, G. Zampella, J.-F. Capon, L. De Gioia, F. Matoussi, S. Mahfoudhi, F.Y. Pétillon, P. Schollhammer and J. Talarmin, *Chem.-Eur. J.*, 2012, **18**, 11123-11138.

25 C. Greco, P. Fantucci, L. De Gioia, R. Suarez-Bertoa, M. Bruschi, J. Talarmin and P. Schollhammer, *Dalton Trans.*, 2010, **39**, 7320-7329.

26 F. I. Adam, G. Hogarth, I. Richards and B. E. Sanchez, *Dalton Trans*., 2007 2495-2498.

27 F. I. Adam, G. Hogarth and I. Richards, *J. Organomet. Chem*., 2007, **692**, 3957-3968.

28 F. I. Adam, G. Hogarth, S. E. Kabir and I. Richards, *C. R. Chim*., 2008, **11**, 890-905.

29 (a) S. Ghosh, G. Hogarth, N. Hollingsworth, K. B. Holt, I. Richards, M. G. Richmond, B. E. Sanchez and D. Unwin, *Dalton Trans*., 2013, **42**, 6775-6792. (b) S. Ghosh, G. Hogarth, N. Hollingsworth, K. B. Holt, S. E. Kabir and B. E. Sanchez, *Chem. Commun*., 2014, **50**, 945-947. (c) S. Ghosh, S. Rana, N. Hollingsworth, M. G. Richmond, S. E. Kabir and G. Hogarth, *Inorganics*, 2018, **6**, 122-135.

30 (a) S. Ghosh, A. Rahaman, K.B. Holt, E. Nordlander, M.G. Richmond, S.E. Kabir and G. Hogarth, *Polyhedron*, 2016, **116**, 127-135. (b) F. Ridley, S. Ghosh, G. Hogarth, N. Hollingsworth, K. B. Holt and D. G. Unwin, J. *Electroanal. Chem*., 2013, **703**, 14-22.

31 S. Ghosh, B.E. Sanchez, I. Richards, M.N. Haque, K.B. Holt, M.G. Richmond and G. Hogarth, *J. Organomet. Chem*., 2016, **812**, 247-258.

32 (a) S. Rana, S. Ghosh, M. K. Hossain, A. Rahaman, G. Hogarth and S. E. Kabir, *Trans. Met. Chem.*, 2016, **41**, 933-942. (b) S. Ghosh, S. E. Kabir and G. Hogarth, *Trans. Met. Chem.*, 2017, **42**, 597-603.

33 A. K Justice, G. Zampella, L. De Gioia, T. B. Rauchfuss, J. I. van der Vlugt and S. R. Wilson, *Inorg. Chem*., 2007, **46**, 1655-1664.

34 N. Wang, M. Wang, T. Liu, T. Zhang and M. Darensbourg, L. Sun, *Inorg. Chem*., 2008, **47**, 6948-6955.

35 P.-H.Zhao, M.-Y. Hu, J.-R. Li, Z.-Y. Ma, Y.-Z. Wang, J. He, Y.-L. Li and X.-F. Liu, *Organometallics*, 2019, **38**, 385-394.

36 P.-H. Zhao, Z.-Y. Ma, M.-Y. Hu, J. He, Y.-Z. Wang, X.-B. Jing, H.-Y. Chen, Z. Wang and Y.-L. Li, *Organometallics*, 2018, **37**, 1280-1290.

37 G. Hogarth and I. Richards, *Inorg. Chem. Commun*., 2007, **10**, 66-70.

38 W. Hewertson and H.R. Watson, *J. Chem. Soc*., 1962, 1490-1494.

39 D.L. Dubois, A. Miedaner and R.C. Haltiwanger, *J. Am. Chem. Soc*., 1991, **113**, 8753-8764.

40 A. Jablonskyté, J.A. Wright, S.A. Fairhurst, J.N.T. Peck, S.K. Ibrahim, V.S. Oganesyan and C.J. Pickett, *J. Am. Chem. Soc.*, 2011, **133**, 18606-18609.

41 A. Jablonskyté, J.A. Wright and C.J. Pickett, *Eur. J. Inorg. Chem*., 2011, 1033-1037.

42 A. Jablonskyté, J.A. Wright and C.J. Pickett, *Dalton Trans*., 2010, **39**, 3026-3034.

43 J.A. Wright and C.J. Pickett, *Chem. Commun*., 2009, 5719-5721.

44 C. Liu, J.N.T. Peck, J.A. Wright, C.J. Pickett and M.B. Hall, *Eur. J. Inorg. Chem*., 2011, 1080-1093.

45 J.A. Wright, L. Webster, A. Jablonskyté, P.M. Woi, S.K. Ibrahim and C.J. Pickett, *Faraday Discuss.*, 2011, **148**, 359-371.

46 M.G.I. Galinato, C.M. Whaley, D. Roberts, P. Wang and N. Lehnert, *Eur. J. Inorg. Chem*., 2011, 1147-1154.

47 S.L. Matthews and D.M. Heinekey, *Inorg. Chem*., 2010, **49**, 9746-9748.

48 A. Jablonskyté, L.R. Webster, T.R. Simmons, J.A. Wright and C.J. Pickett, *J. Am. Chem. Soc.*, 2014, **136**, 13038-13044.

49 L. Schwartz, G. Eilers, L. Eriksson, A. Gogoll, R. Lomoth and S. Ott, *Chem. Commun*., 2006, 520–522.

50 G. Eilers, L. Schwartz, M. Stein, G. Zampella, L. De Gioia, S. Ott and R. Lomoth, *Chem. Eur. J.*, 2007, **13**, 7075–7084.

51 S. Ott, M. Kritikos, B. Åkermark, L. Sun and R. Lomoth, *Angew. Chem., Int. Ed*., 2004, **43**, 1006–1009.

52 F. Wang, M. Wang, X. Liu, K. Jin, W. Dong, G. Li, B. Åkermark and L. Sun, *Chem. Commun.*, 2005, 3221–3223.

53 J.-F. Capon, S. Ezzaher, F. Gloaguen, F. Y. Pétillon, P. Schollhammer and J. Talarmin, *Chem.–Eur. J*., 2008, **14**, 1954–1964.

54 H. Li and T. B. Rauchfuss, *J. Am. Chem. Soc*., 2002, **124**, 726–727.

55 S. Jiang, J. Liu, Y. Shi, Z. Wang, B. Åkermark and L. Sun, *Dalton Trans*., 2007, 896–902.

56 G. Zampella, P. Fantucci and L. De Gioia, *Chem. Commun.*, 2010, 8824-8826.

57 A.R. Finkelmann, M.T. Stiebritz and M. Reiher, *Chem. Sci.*, 2014, **5**, 215-221.

58 (a) W. Wang, M.J. Nilges, T.B. Rauchfuss and M. Stein, *J. Am. Chem. Soc*., 2013, **135**, 3633-3639. (b) Y.-C. Liu, K.-T. Chu, Y.-L. Huang, C.-H. Hsu, G.-H. Lee, M.-C. Tseng and M.-H. Chiang, *ACS Catalysis*, 2016, **6**, 2559-2576.

59 T. Liu and M.Y. Darensbourg, *J. Am. Chem. Soc*., 2007, **129**, 7008-7009.

60 C.M. Thomas, T. Liu, M.B. Hall and M.Y. Darensbourg, *Inorg. Chem*., 2008, **47**, 7009-7024.

61 M.R. Carlson, D.L. Gray, C.P. Richers, W. Wang, P.-H. Zhao, T.B. Rauchfuss, V. Pelmenschikov, C.C. Pham, L.B. Gee, H. Wang and S.P. Cramer, *Inorg. Chem*., 2018, **57**, 1988-2001.

61 S. Ezzaher, J.-F. Capon, N. Dumontet, F. Gloaguen, F.Y. Petillon and P. Schollhammer, J. Talarmin, *J. Electroanal. Chem*., 2009, **626**, 161-170.

63 M.G. Basallote, M. Besora, C.E. Castillo, M.J. Fernández-Trujillo, A. Lledós, F. Maseras and M.A. Máñez, *J. Am. Chem. Soc*., 2007, **129**, 6608-6618.

64 A.G. Algarra, M.G. Basallote, M.J. Fernández-Trujillo, R. Llusar, V.S. Safont and C. Vicent, *Inorg. Chem*., 2006, **45**, 5774-5784.

65 M.E. Carroll, B.E. Barton, T.B. Rauchfuss and P.J. Carroll, *J. Am. Chem. Soc.*, 2012, **134**, 18843-18852.

66 B.E. Barton and T.B. Rauchfuss, *Inorg. Chem*., 2008, **47**, 2261-2263.

67 A.K. Justice, M.J. Nilges, T.B. Rauchfuss, S.R. Wilson, L. De Gioia and G. Zampella, *J. Am. Chem. Soc.*, 2008, **130**, 5293-5301.

68 W. Wang, T.B. Rauchfuss, L. Zhu and G. Zampella, *J. Am. Chem. Soc*., 2014, **136**, 5773-5782.

69 M.T. Huynh, W. Wang, T.B. Rauchfuss and S. Hammes-Schiffer, *Inorg. Chem*., 2014, **53**, 10301-10311.

70 R. Zaffaroni, T.B. Rauchfuss, D.L. Gray, L. De Gioia and G. Zampella, *J. Am. Chem. Soc*., 2012, **134**, 19260-19269.

71 A. Winter, L. Zsolnai and G. Huttner, *Zeit. Naturforsch. Teil B: Anorg. Chem. Org. Chem*., 1982, **37**, 1430-1436.

72 J.D. Lawrence, H. Li and T.B. Rauchfuss, *Chem. Commun*., 2001, 1482-1483.

73 R.B. King, *J. Am. Chem. Soc.*, 1962, **84**, 2460.

74 SMART Version 5.628, Bruker AXS, Inc., Analytical X-ray Systems, 5465 East Cheryl Parkway, Madison WI 53711-5373, 2003.

75 SAINT Version 6.36A, Bruker AXS, Inc., Analytical X-ray Systems, 5465 East Cheryl Parkway, Madison WI 53711-5373, 2002.

76 G. M. Sheldrick, SADABS Version 2.10, University of Göttingen, 2003.

77 G. M. Sheldrick, *Acta Cryst.*, 2008, **A64**, 112-122.

78 M.J. Frisch, *et al*., Gaussian 09, Revision E.01, Gaussian, Inc., Wallingford, CT, USA, 2009.

79 A.D. Becke, *J. Chem. Phys*., 1993, **98**, 5648-5652.

80 C. Lee and W. Yang, R.G. Parr, *Phys. Rev. B*, 1993, **37**, 785-789.

81 (a) JIMP2, version 0.091, a free program for the visualization and manipulation of molecules: M.B. Hall and R.F. Fenske, *Inorg. Chem*., 1972, **11**, 768-775. (b) J. Manson, C.E. Webster, M.B. Hall, Texas A&M University, College Station, TX, 2006: http://www.chem.tamu.edu/jimp2/index.html.

Table 2 Crystallographic data and structure refinement for **1-2**

Compound	**1**.CH_2Cl_2	**2**.0.25H_2O
empirical formula	$C_{41}H_{41}O_3Fe_2S_2P_3Cl_2$	$C_{46}H_{44.5}O_{3.25}Fe_2S_2P_3N_1$
formula weight	921.37	932.06
temp (K)	150(2)	150(2)
wavelength (Å)	0.71073	0.71073
crystal system	triclinic	triclinic
space group	P $\bar{1}$	C_2/c
a (Å)	9.4439(8)	47.771(9)
b (Å)	9.6258(9)	11.747(2)
c (Å)	22.437(2)	15.183(3)
α (°)	99.783(1)	90
β (°)	95.331(2)	97.984(4)
γ (°)	94.278(2)	90
Volume (Å^3)	1992.8(3)	8438(3)
Z	2	8
D_{calc} (Mg m^{-3})	1.5369	1.467
μ (Mo Kα) (mm^{-1})	1.1278	0.944
F(000)	948	3860
crystal color	orange	red
crystal size (mm)	0.16 × 0.15 × 0.04	0.14 × 0.13 × 0.09
θ range (°)	1.85−28.29	2.45−28.34
limiting indices	$-12 \le h \ge 12$	$-61 \le h \ge 63$
	$-12 \le k \ge 12$	$-15 \le k \ge 15$
	$-29 \le l \ge 28$	$-20 \le l \ge 20$
structure solution	direct methods	direct methods
reflections collected	17384	356729
independent reflections (R_{int})	9087 (0.0228)	10136 (0.0550)
max. and min. transmission	0.9563 and 0.8403	0.9199 and 0.8792
data/restraints/parameters	9087 / 0 / 478	10136 / 0 / 518
goodness of fit on F^2	1.046	1.049
final *R* indices [$I > 2\sigma(I)$]	R_1 = 0.0405	R_1 = 0.0500
	wR_2 = 0.0950	wR_2 = 0.1107
R indices (all data)	R_1 = 0.0510	R_1 = 0.0736
	wR_2 = 0.0998	wR_2 = 0.1203
largest diff. peak and hole (e Å^{-3})	1.659 and −1.013	0.707 and −0.497

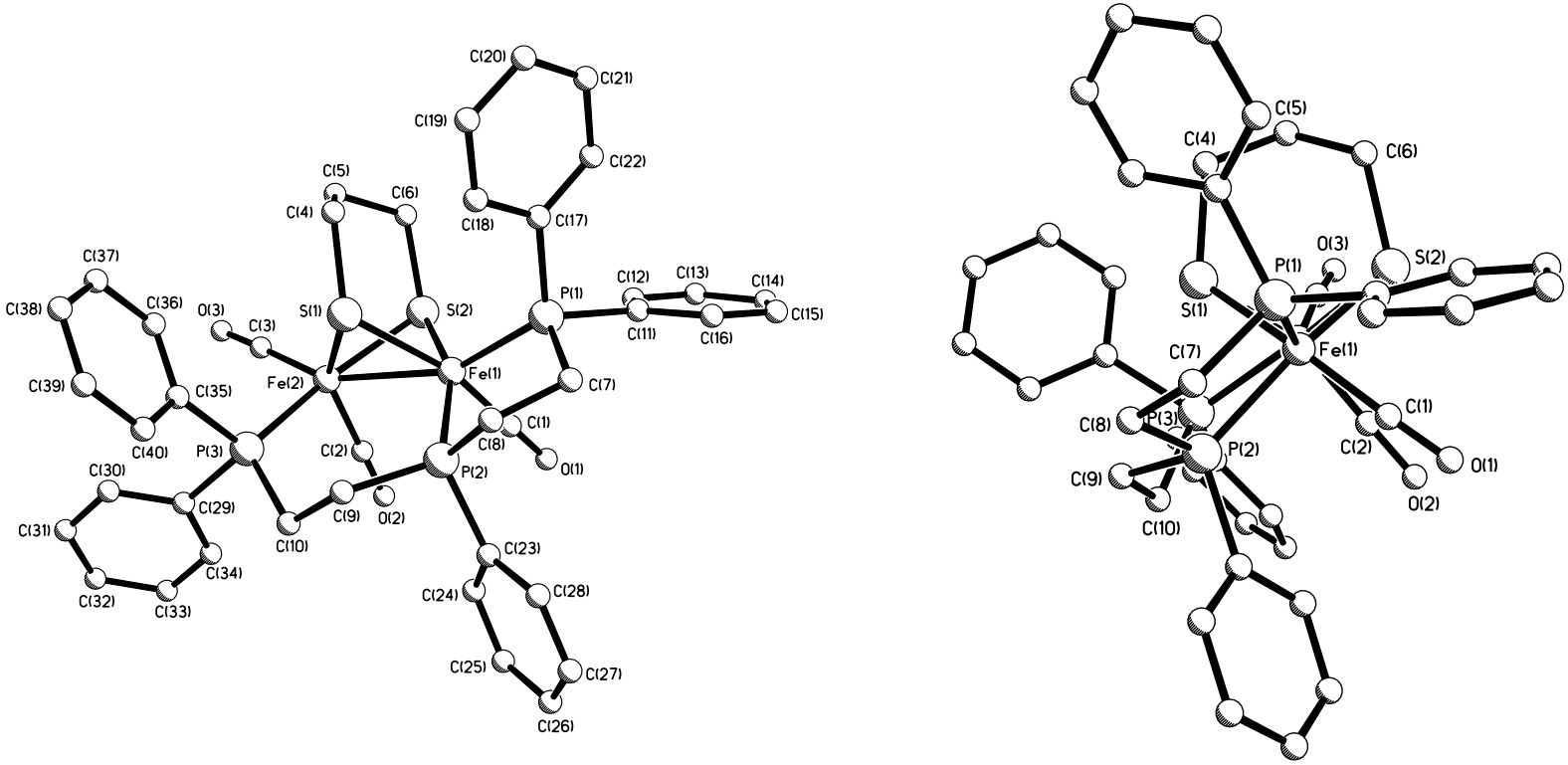

Figure 1. Two views of the molecular structure of $Fe_2(CO)_3(\mu\text{–pdt})(\mu,\kappa^1,\kappa^2\text{-triphos})$ (**1**)

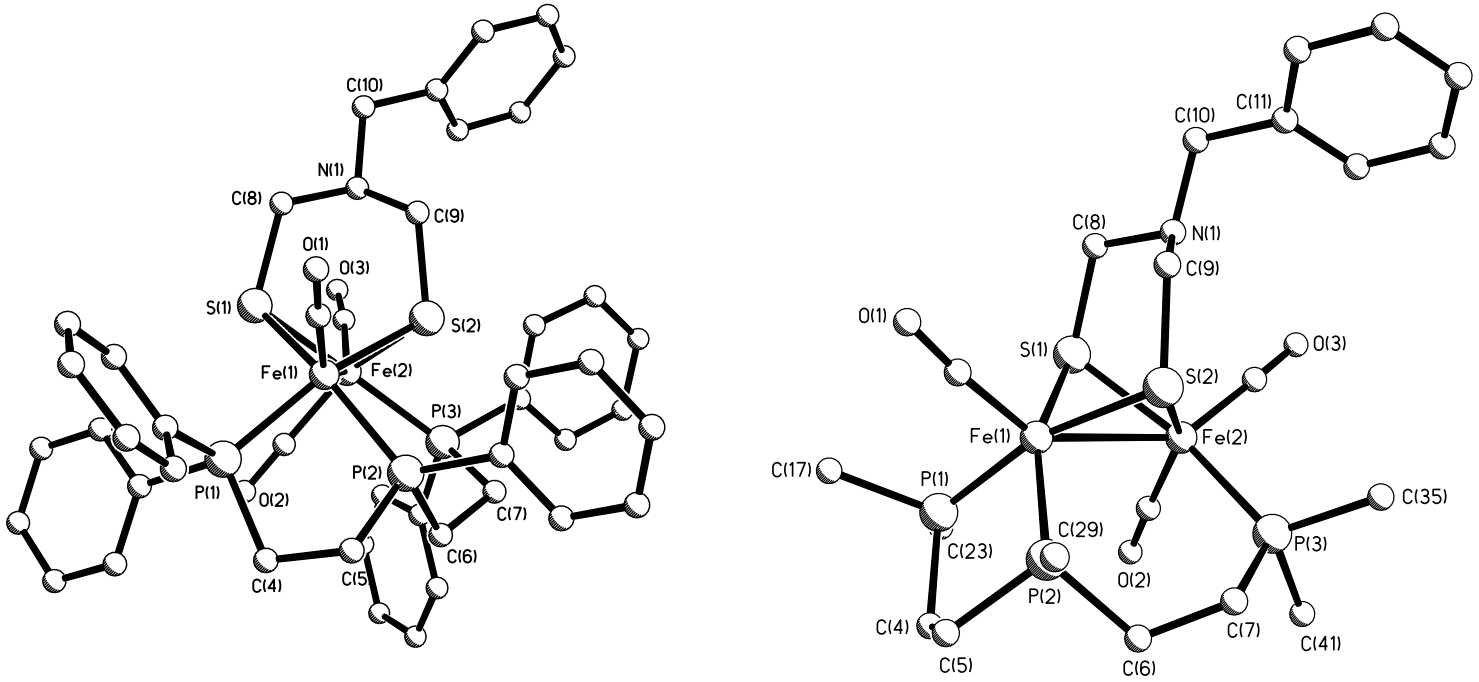

Figure 2. Two views of the molecular structure of $Fe_2(CO)_3(\mu\text{-adt})(\mu,\kappa^1,\kappa^2\text{-triphos})$ (**2**)

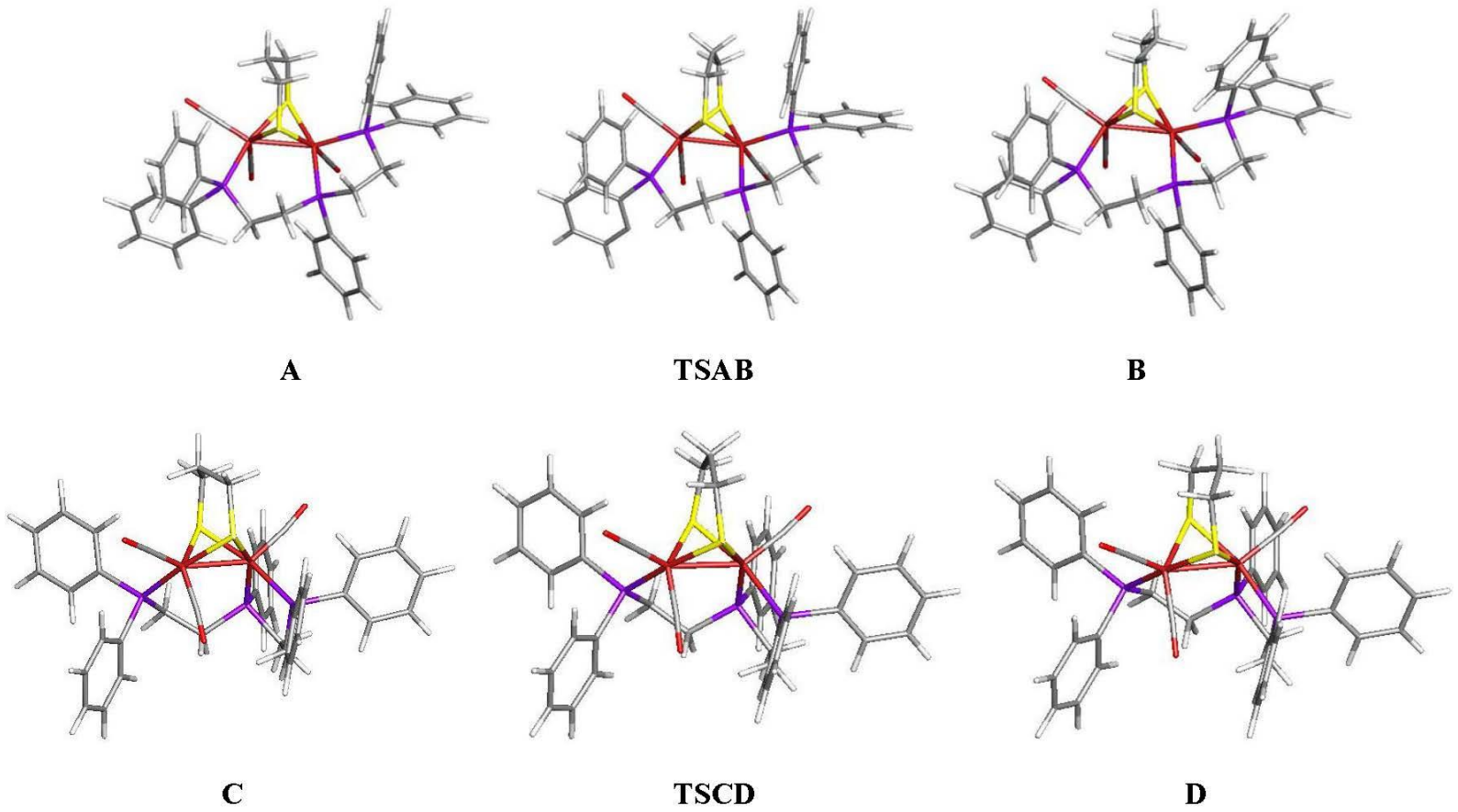

Figure 3. Optimised B3LYP structures for the stereoisomers **A** through **D**, and the corresponding transition-state structures **TSAB** and **TSCD**.

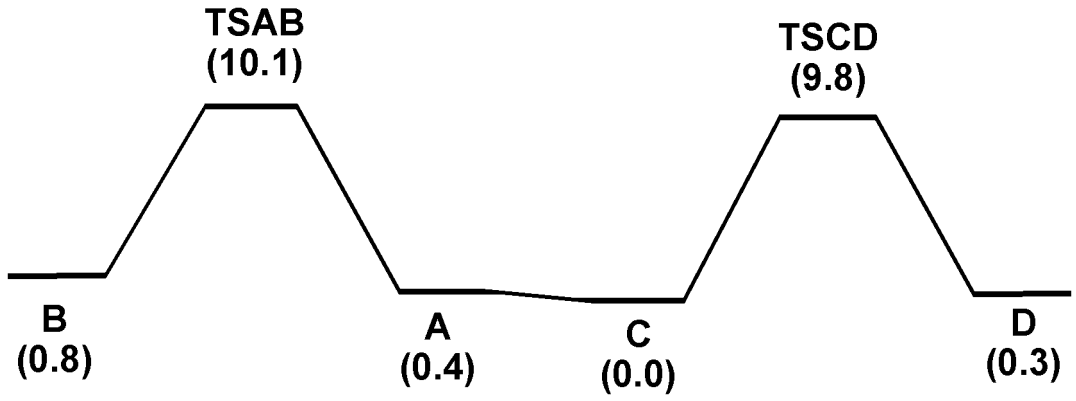

Figure 4. B3LYP potential energy surface for the ground-state energy difference between **1bba** (**A**) and **1bbb** (**C**) and energetics for pdt ring flipping. Energy values are in ΔG in kcal/mol relative to species **C**.

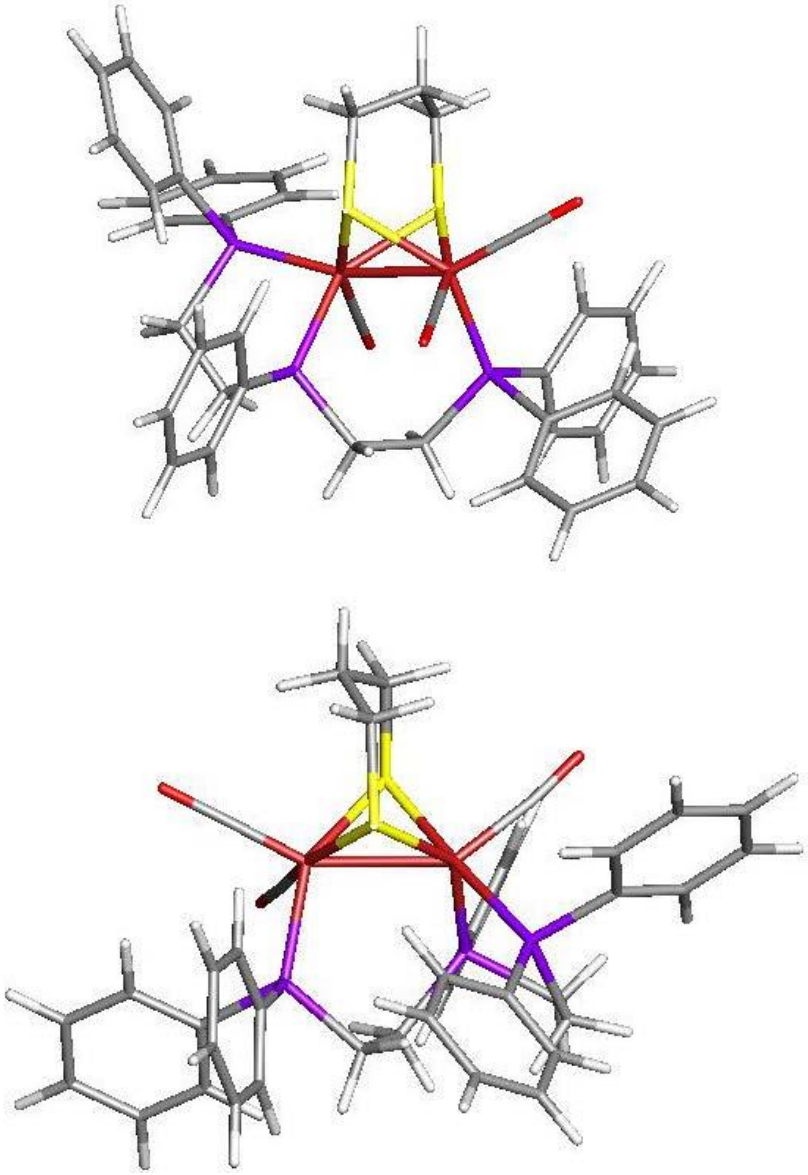

Figure 5. B3LYP-optimised structures of **A_Alt** (top) and **C_Alt** (bottom).

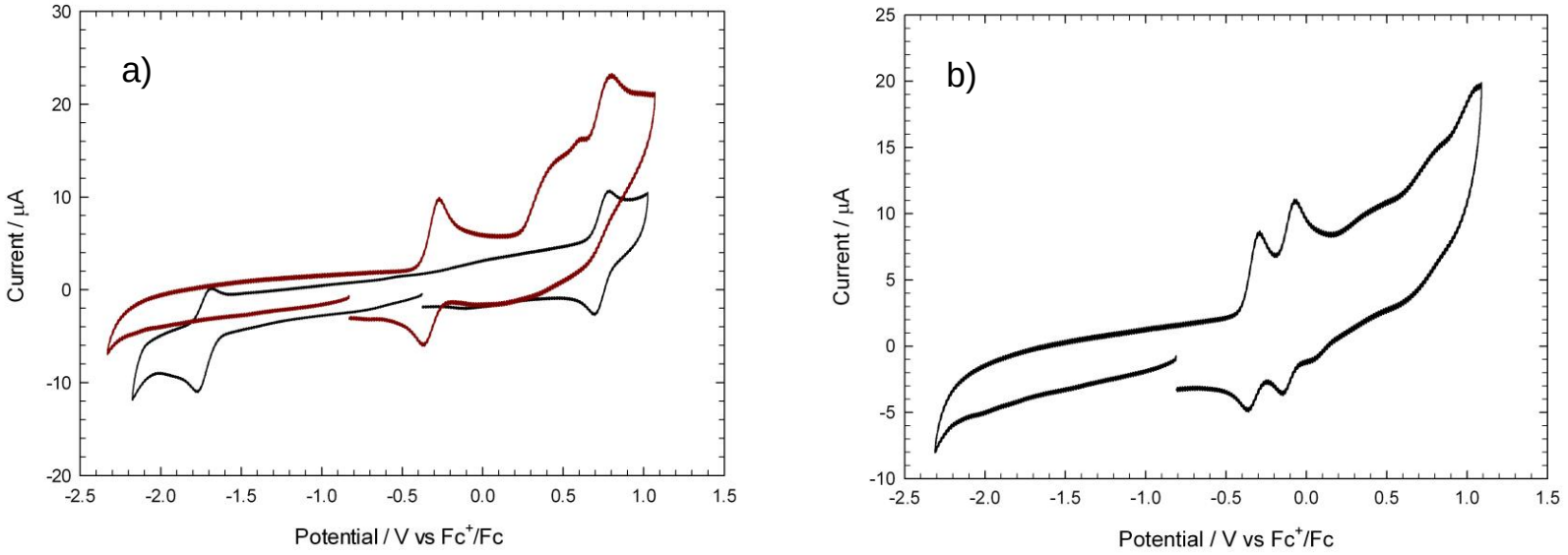

Figure 6. (a) CV of 0.5 mM **1** (brown trace) and 0.5 mM **1H**$^{+}$ (black trace) and (b) **3** in CH_2Cl_2/0.1 M $TBAPF_6$ (scan rate = 0.1 V s^{-1}; TBA = tetrabutylammonium)

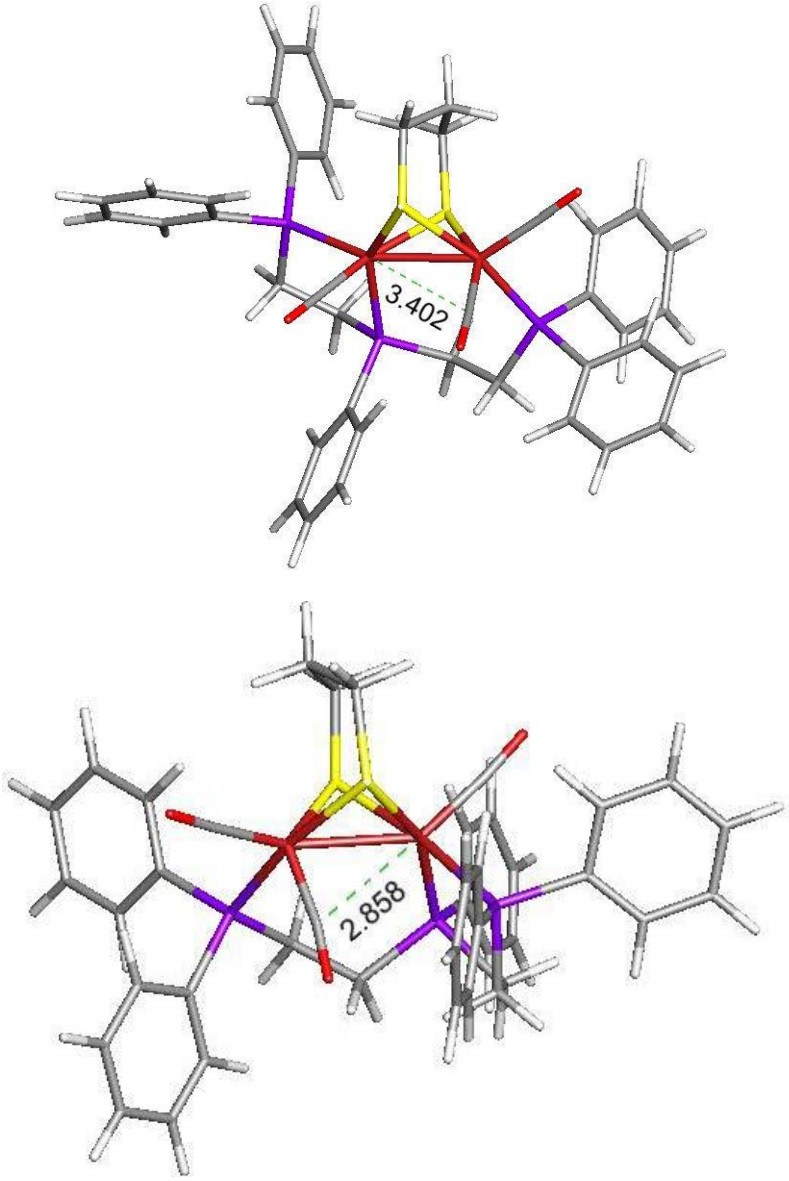

Figure 7. B3LYP-optimised structures of the radical cation structures $\mathbf{A_{ox}}$ (top) and $\mathbf{C_{ox}}$ (bottom).

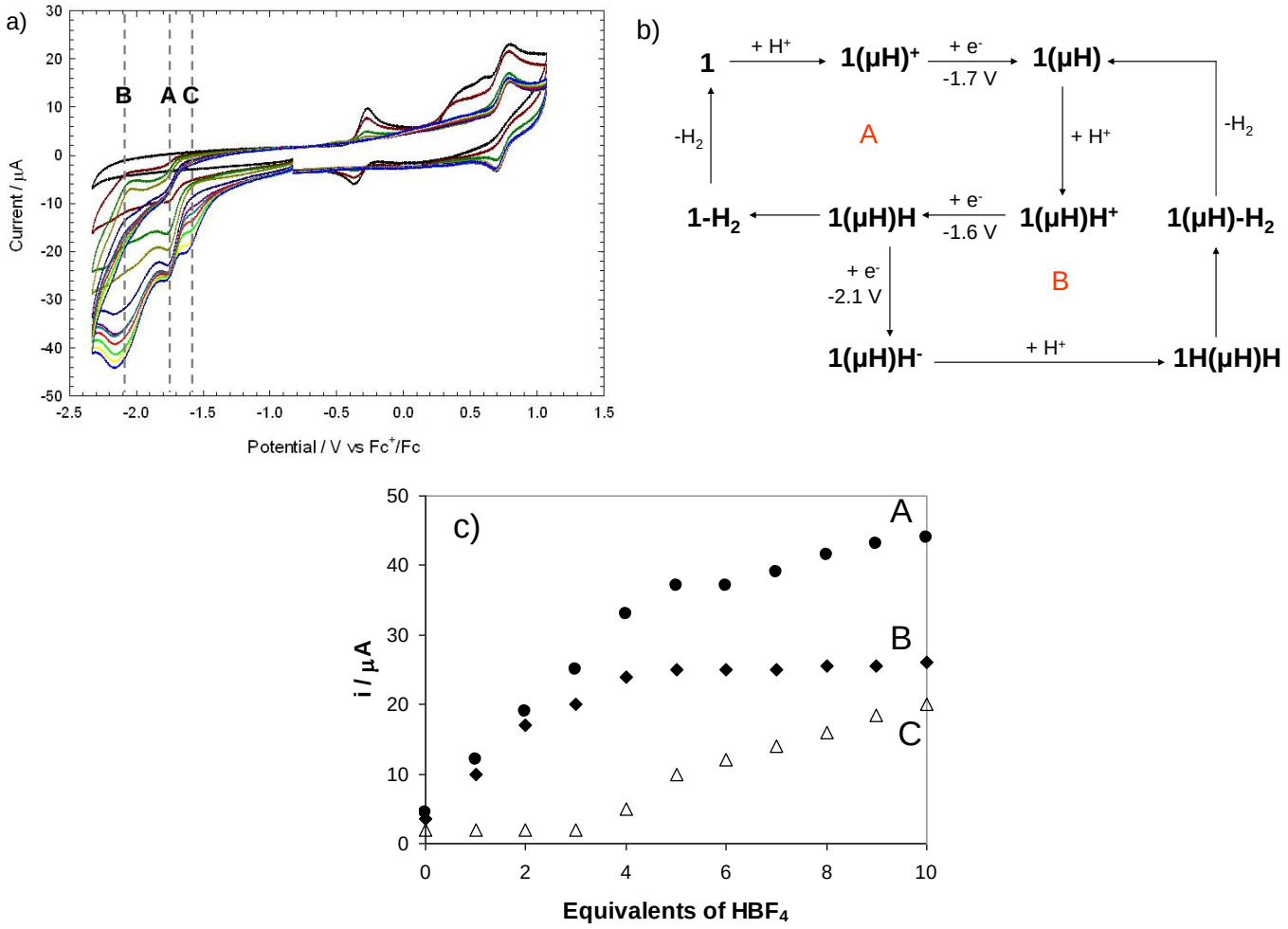

Figure 8. (a) CV of 0.5 mM **1** in 0.1 M $TBAPF_6$ / CH_2Cl_2 (black trace) and in the presence of increasing (1-10) molar equivalents of $HBF_4{\cdot}Et_2O$. **A**, **B** and **C** refer to catalytic processes discussed in the text; (b) Proposed catalytic cycles giving rise to currents at **A** and **B**; (c) Plot of limiting current at potentials **A** (solid circles), **B** (solid diamonds) and **C** (open triangles) with addition of molar equivalents of HBF_4.

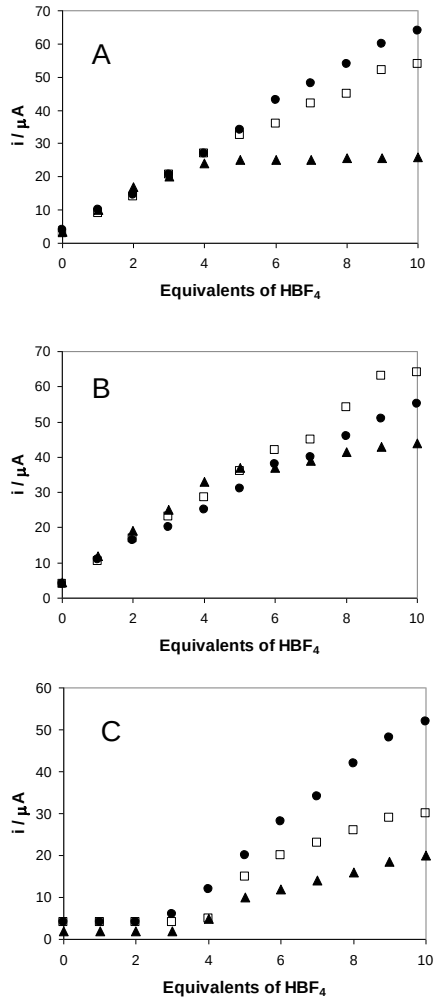

Figure 9. Plots of limiting current at potentials **A** (top) **B** (middle) and **C** (bottom) with addition of molar equivalents of $HBF_4 \cdot Et_2O$ for 0.5 mM **1** in CH_2Cl_2 with 0.1 M $TBAPF_6$ (closed triangles); 0.1 M $TBABF_4$ (open squares) and 0.1 M $TBAClO_4$ (closed circles).

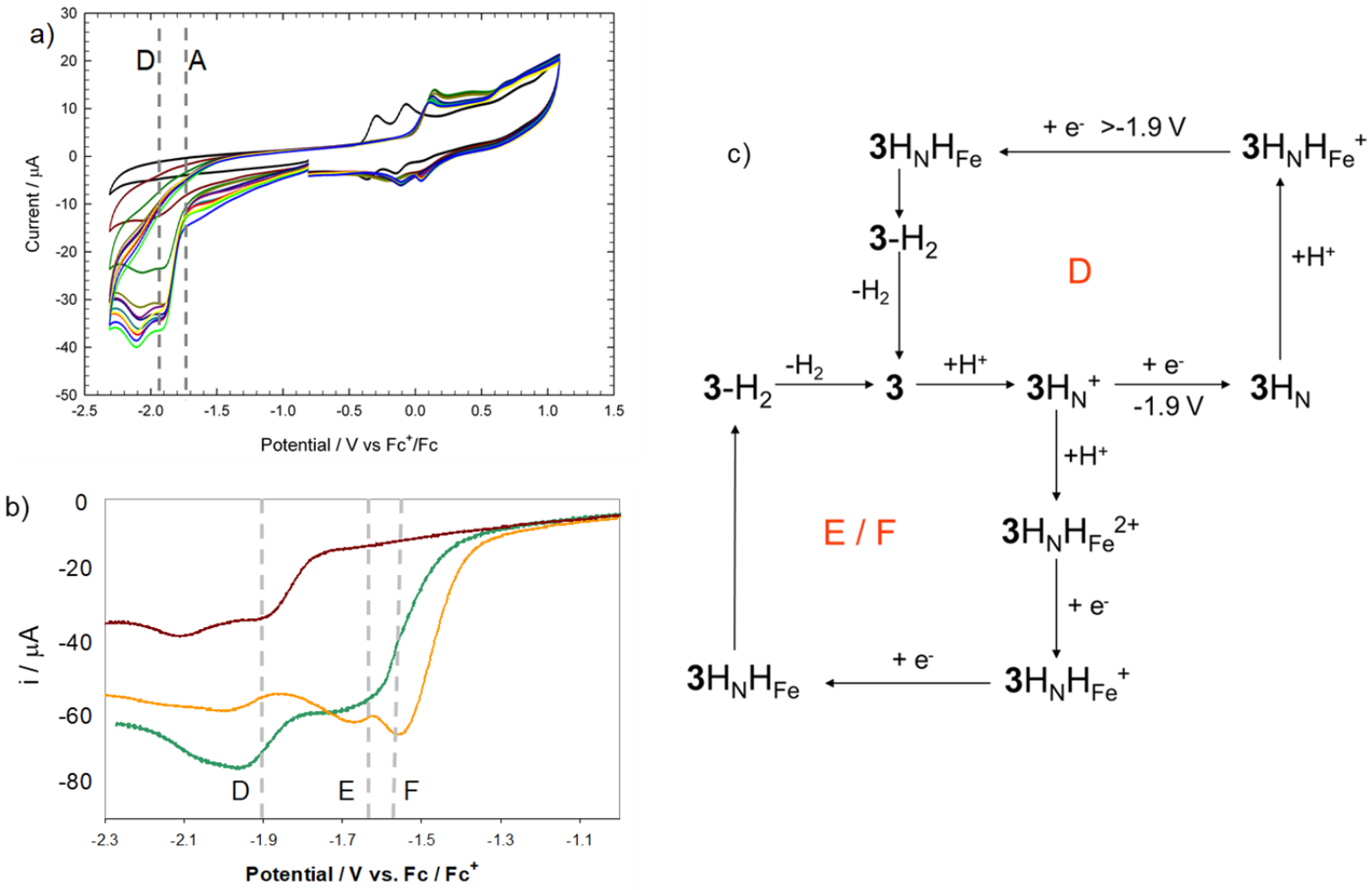

Figure 10. a) CV of 0.5 mM **3** in 0.1 M $TBAPF_6$ / CH_2Cl_2 (black trace) and in the presence of increasing (1-10) molar equivalents of $HBF_4{\cdot}Et_2O$. **A** and **D** refer to catalytic processes discussed in the text; b) Forward scan of CV of 0.5 mM **3** and 5 mM $HBF_4{\cdot}Et_2O$ in CH_2Cl_2 with 0.1 M $TBAPF_6$ (brown trace), 0.1 M $TBABF_4$ (green trace) and 0.1 M $TBAClO_4$ (orange trace). **D**, **E** and **F** refer to catalytic processes discussed in the text; c) Proposed catalytic cycles giving rise to currents at **D**, **E** and **F**, potentials for reduction steps for cycle **E** / **F** not shown.